Article

S-acylation of ATGL is required for lipid droplet homoeostasis in hepatocytes

🔴 Check for updates

Yuping Zheng [1,9], Jishun Chen [2,9], Vinitha Macwan [3,9], Charneal L. Dixon [4,5,9], Xinran Li [6], Shengjie Liu [7], Yuyun Yu[1], Pinglong Xu [8], Qiming Sun[1], Qi Hu [7], Wei Liu [1] ✉, Brian Raught [3] ✉, Gregory D. Fairn [4,5] ✉ & Dante Neculai [1] ✉

Lipid droplets (LDs) are organelles specialized in the storage of neutral lipids, cholesterol esters and triglycerides, thereby protecting cells from the toxicity of excess lipids while allowing for the mobilization of lipids in times of nutrient deprivation. Defects in LD function are associated with many diseases. S-acylation mediated by zDHHC acyltransferases modifies thousands of proteins, yet the physiological impact of this post-translational modification on individual proteins is poorly understood. Here, we show that zDHHC11 regulates LD catabolism by modifying adipose triacylglyceride lipase (ATGL), the rate-limiting enzyme of lipolysis, both in hepatocyte cultures and in mice. zDHHC11 S-acylates ATGL at cysteine 15. Preventing the S-acylation of ATGL renders it catalytically inactive despite proper localization. Overexpression of zDHHC11 reduces LD size, whereas its elimination enlarges LDs. Mutating ATGL cysteine 15 phenocopies zDHHC11 loss, causing LD accumulation, defective lipolysis and lipophagy. Our results reveal S-acylation as a mode of regulation of ATGL function and LD homoeostasis. Modulating this pathway may offer therapeutic potential for treating diseases linked to defective lipolysis, such as fatty liver disease.

The accumulation of lipid droplets (LDs) is the hallmark of various human diseases, including atherosclerosis, nonalcoholic fatty liver disease and obesity. These conditions result from nutritional excess, as the proliferation and enlargement of LDs prevent the toxic build-up of lipids in other organelles[1–4]. Indeed, LD size and abundance are intimately coupled to the metabolic state of the cell[3]. In response to metabolic signals, mobilized fatty acids derived from stored neutral lipids are involved in many cell functions, including energy production through β-oxidation, membrane biogenesis to support cell division, protein modification, signal transduction and lipoprotein secretion[1,5,6].

Thus, understanding the balance between LD biogenesis and catabolism and its dysregulation in the aetiology of metabolic conditions such as type 2 diabetes is crucial for developing new therapeutic strategies[7–9].

The hydrolysis of triacylglycerol (TAG) in LDs to three fatty acids and glycerol is catalysed by the sequential actions of three enzymes: adipose triacylglyceride lipase (ATGL; also known as PNPLA2)[10,11], a member of the patatin-like phospholipase domain-containing protein A (PNPLA) family; hormone-sensitive lipase (HSL)[12]; and monoglyceride lipase[6,12]. ATGL catalyses the initial and the rate-limiting step in the mobilization of fatty acids stored as TAGs and is subjected to multiple

[1]Center for Metabolism Research, The Fourth Affiliated Hospital of School of Medicine and International School of Medicine, International Institutes of Medicine, Zhejiang University, Yiwu, China. [2]Department of Cell Biology, Zhejiang University School of Medicine, Hangzhou, China. [3]Princess Margaret Cancer Centre, University Health Network, Toronto, Ontario, Canada. [4]Keenan Research Centre for Biomedical Science, St. Michael's Hospital, University Health Network, Toronto, Ontario, Canada. [5]Department of Pathology, Dalhousie University, Halifax, Nova Scotia, Canada. [6]ZJU-Hangzhou Global Scientific and Technological Innovation Center, Hangzhou, China. [7]Westlake AI Therapeutics Lab, Westlake Laboratory of Life Sciences and Biomedicine, School of Life Sciences, Westlake University, Hangzhou, China. [8]Life Science Institute, Zhejiang University, Hangzhou, China. [9]These authors contributed equally: Yuping Zheng, Jishun Chen, Vinitha Macwan, Charneal L. Dixon. ✉e-mail: liuwei666@zju.edu.cn; brian.raught@uhnresearch.ca; gfairn@dal.ca; dneculai@zju.edu.cn
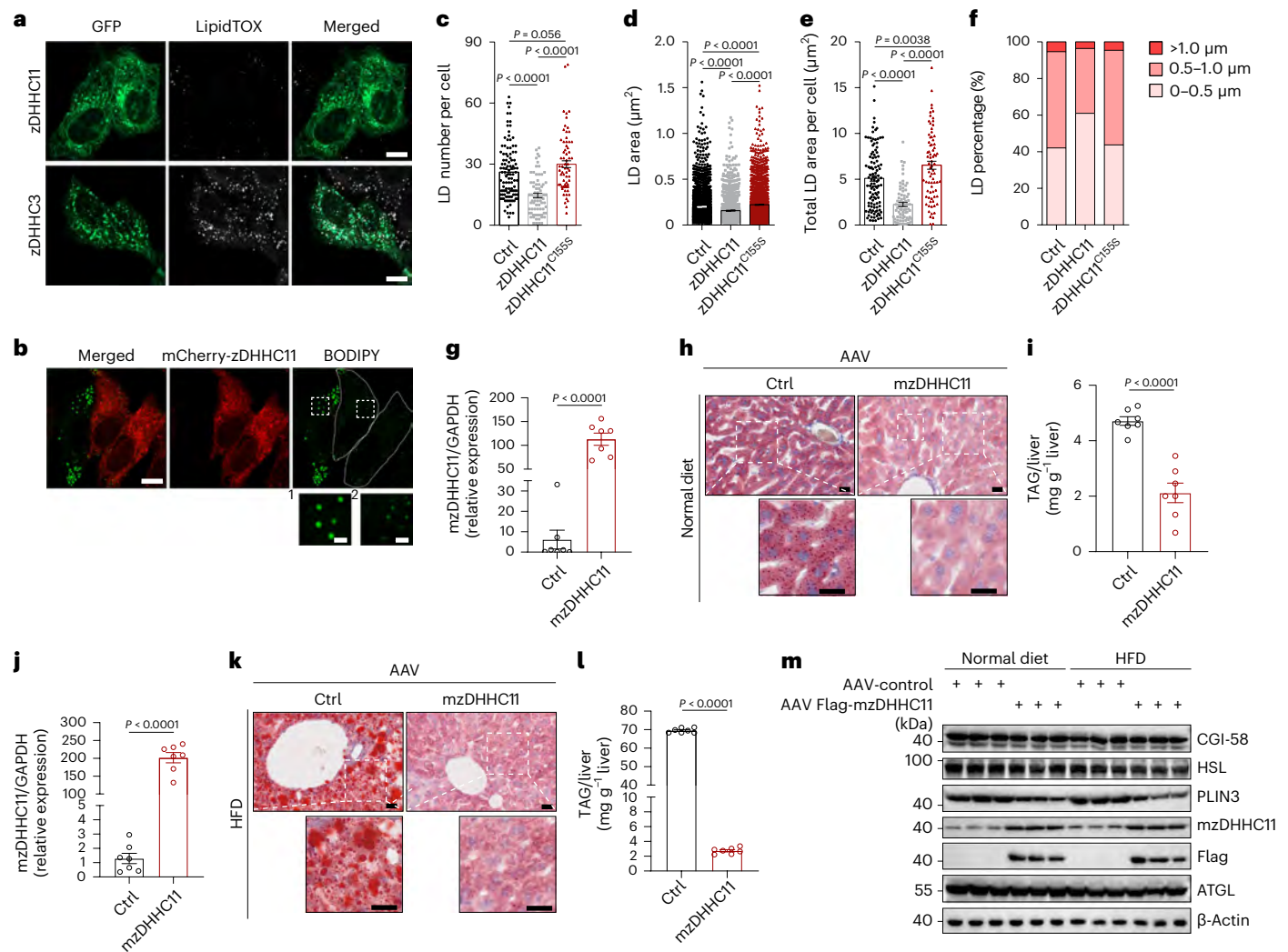
Fig. 1 | Overexpression of zDHHC11 reduces LD size and abundance in HepG2 cells and mouse livers. a, Fluorescence microscopy images of HepG2 cells expressing GFP-tagged zDHHC3 or zDHHC11, with LDs visualized using LipidTOX Red staining. **b**, Confocal images of HepG2 cells transfected with mCherry-zDHHC11; LDs were highlighted with BODIPY 493/503. Specifically, inset 1 in **b** depicts an untransfected cell, whereas inset 2 depicts a cell expressing mCherry-zDHHC11. **c**–**f**, Quantitative data derived from similar images as in **b** across three independent experiments, including the number of LDs per cell (**c**), the cross-sectional area of individual LDs (**d**), the total LD area per cell (**e**) and the percentage distribution of LDs based on diameter (**f**). Sample sizes: $n = 44$ for control (Ctrl) HepG2 cells, $n = 76$ for HepG2 cells with zDHHC11 overexpression and $n = 77$ for HepG2 cells expressing the catalytically inactive zDHHC11^{C155S} variant. **g**,**j**, RT–qPCR analysis determining zDHHC11 expression levels in the livers of male C57BL/6J mice; the mice were injected with either the AAV-control virus or the AAV-mzDHHC11 virus and then maintained on a standard diet (**g**) or an HFD (**j**) ($n = 7$ per group). **h**,**k**, Representative liver sections from mice fed a standard diet (**h**) or an HFD (**k**), stained with Oil Red O. **i**,**l**, Quantification of the total triglyceride content in liver samples from mice fed a standard diet (**i**) or an HFD (**l**). **m**, Immunoblot analysis comparing the expression of CGI-58, HSL, PLIN3, zDHHC11, ATGL and β-actin in individual liver samples from the mice in **g** and **j**, with each lane representing a separate biological replicate (individual mouse). Data in **c**, **d**, **e**, **g**, **i**, **j** and **l** are presented as mean ± s.e.m. and analysed with one-way ANOVA and Tukey's post hoc tests (**c**–**e**) or an unpaired two-tailed Student's t test (**g**, **i**, **j** and **l**). Scale bars are 10 μm for **a** and **b** (2 μm for insets in **b**) and 100 μm for **h** and **k** (100 μm for insets).

levels of regulation[5,6]. ATGL is regulated by direct interaction with its coactivator, the LD-binding protein comparative gene identification-58 (CGI-58)[13], and its inhibitor, G0/G1 switch protein 2 (G0S2)[14]. During nutrient depletion, ATGL is also regulated by phosphorylation (at Ser406) by AMP-activated protein kinase (AMPK)[15] or protein kinase A (PKA)[15,16]. Following the liberation of the three fatty acyl chains, these molecules can be converted to acyl-CoA by the acyl-CoA synthetase family for further use in additional metabolic pathways, including phospholipid synthesis and β-oxidation[5].

Palmitoyl-CoA and other acyl-CoAs are also used as substrates for the lipidation of proteins. For instance, acyl-CoAs serve as a substrate for the S-acyltransferases of the zDHHC family that post-translationally attach fatty acids (that is, palmitate) to proteins. Roughly 10%

of the proteome undergoes S-palmitoylation (or S-acylation) by modifying cysteine residues with palmitate (or other fatty acids). Mass spectrometry-based methods have revealed that human diseases, including immunological and neurodegenerative disorders, cancers and viral infections, are associated with alterations in the S-palmitoylome[17,18]. Protein S-acylation is reversible and can dynamically modulate protein stability and protein–protein interactions, enzymatic activities and localization, including proteins associated with LDs. Multiple LD proteins are S-acylated. For example, S-palmitoylation of the ADP-ribosylation factor GTPase-activating protein ELMOD2 by zDHHC3 is required to target LDs and for proper LD homoeostasis[19]. The LD-associated small G proteins Rab18 (ref. 20) and Rab10 (ref. 21) are also S-palmitoylated. To date, the extent and

importance of the role of zDHHC enzymes and S-acylation in LD physiology are unclear.

We postulated that critical proteins involved in LD homoeostasis are potentially S-acylated (or palmitoylated) and that zDHHC family members may influence fatty acid and TAG metabolism. Therefore, we conducted a targeted overexpression and genetic silencing screening to determine whether any of the zDHHC proteins affect LD homoeostasis. Our results demonstrate that zDHHC11 influences LD homoeostasis by modifying and activating ATGL.

Results

zDHHC11 acyltransferase affects LD size and abundance

To delve deeper into the role of protein S-acylation in LD function, we overexpressed 23 green fluorescent protein (GFP)-tagged zDHHC enzymes individually in HepG2 cells. We then monitored the size and abundance of LDs using LipidTOX (Fig. 1a and Extended Data Fig. 1a). Although previous studies have indicated a potential role for zDHHC3 in LD physiology[19], our confocal microscopy analysis revealed that the overexpression of zDHHC11 had the most pronounced effect on LD size and abundance (Fig. 1a and Extended Data Fig. 1a). In line with this, HepG2 and Huh7 cells expressing mCherry-zDHHC11 (which localized to the endoplasmic reticulum (ER), as shown in Extended Data Fig. 1b) and AML12 cells expressing mCherry-mzDHHC11 exhibited fewer and smaller LDs compared with their nontransfected counterparts (Fig. 1b and Extended Data Fig. 1c–e). Both the cross-sectional area of individual LDs and the total LD area per cell were significantly reduced compared with cells overexpressing mCherry alone (Fig. 1c–f). To ascertain whether the observed phenotype depended on zDHHC11's transferase activity, we conducted experiments with a catalytically inactive zDHHC11 (C155S) mutant. Transient overexpression of this mutant in HepG2 cells did not alter LD size or count (Fig. 1c–f). Hence, ER-localized zDHHC11-mediated S-acylation influences LD homoeostasis in cultured human cells.

To see whether these observations held in vivo, we overexpressed *Zdhhc11* in C57BL/6J mice using a liver-targeted adeno-associated virus (AAV). *Zdhhc11* transcript levels were assessed by reverse transcription followed by qPCR (RT–qPCR) (Fig. 1g,j). Control and *Zdhhc11*-overexpressing male mice (aged 6–8 weeks, with a minimum of six mice in each group) were fed either standard chow or a high-fat diet (HFD) for 3 months. Subsequent analysis of liver sections using histology and Oil Red O staining showed that liver samples from *Zdhhc11*-overexpressing male mice exhibited a significant reduction in the number of LDs and TAG content, regardless of diet type (Fig. 1h,i,k,l). Similarly, *Zdhhc11*-overexpressing female mice also exhibited significant reductions in LDs and TAG content when fed a chow diet (Extended Data Fig. 1f–h). Consistent with previous reports, female mice were resistant to HFD-induced weight gain and steatosis[22,23]. For subsequent studies, only male mice were used. Livers from *Zdhhc11*-overexpressing mice demonstrated a marked decrease in the levels of perilipin 3 (PLIN3) (Fig. 1m and Extended Data Fig. 1i), an LD coat protein whose abundance correlates to LD content and facilitates triglyceride storage and lipolysis[5,24]. Meanwhile, other proteins transiently associated with LDs, such as HSL[5], CGI-58 (ref. [5]) or ATGL, showed no significant differences (Fig. 1m and Extended Data Fig. 1i). These findings highlight the critical role of zDHHC11 in LD homoeostasis.

ZDHHC11 loss enhances LD size, abundance and TAG content

Motivated by the observed effect of zDHHC11 overexpression on LDs, we next examined the impact of loss of zDHHC11 activity on LDs. The human genome contains a duplicated version of *ZDHHC11* (*ZDHHC11* and *ZDHHC11B*) encoding proteins with 86% sequence identity. For silencing or knockout (KO) studies, we targeted both *ZDHHC11* and *ZDHHC11B* (hereafter denoted *ZDHHC11+(B)*). Compared with HepG2 or mouse embryonic fibroblast (MEF) cells expressing control short

hairpin RNA (shRNA), the expression of shZDHHC11+(B) (blue fluorescent protein (BFP)-positive cells) (Extended Data Fig. 2a–c) correlated with increased LD size and abundance (Extended Data Fig. 2d,f–j). The transient silencing also increased intracellular TAG levels (Extended Data Fig. 2e) and decreased basal lipolysis (Extended Data Fig. 2k). Similar results were observed in a clustered regularly interspaced short palindromic repeats (CRISPR)/CRISPR-associated protein 9 (Cas9)-engineered *ZDHHC11+(B)*-KO HepG2 cell line (HepG2[zDHHC11+(B)-KO]) (Fig. 2a–g), which we generated and authenticated (Extended Data Fig. 2l–n). Thus, toggling the levels of the zDHHC11 protein up or down results in a decrease or increase in LDs, respectively.

In prior experiments, we used a standard medium fortified with 10% FBS and high glucose concentrations. When we introduced exogenous fatty acids, specifically the oleate (OA)/BSA complex, both the HepG2 and HepG2[zDHHC11+(B)-KO] cell lines displayed a significant increase in TAG production, evident from the expanded total LD area per cell, compared with those treated solely with BSA. Following culturing with OA/BSA for 4 h, these cells exhibited notably more prominent and numerous LDs than cells cultured in a standard medium supplemented with BSA (Extended Data Fig. 2o,p). Interestingly, the OA-induced enhancement was especially noticeable in *ZDHHC11*-KO cells. This suggests that loss of zDHHC11 activity may have a role in boosting LD expansion. Therefore, we considered whether zDHHC11 acts as a negative regulator of de novo LD formation and subsequent expansion or influences LD catabolism. We took advantage of a synthetic construct termed LiveDrop, a marker of newly formed neutral lipid-poor LDs, based on the membrane-embedded hairpin motif from glycerol-3-phosphate acyltransferase 4 (GPAT4) linked to a fluorescent tag[1]. For this experiment, LiveDrop-labelled wild-type (WT) and HepG2[zDHHC11+(B)-KO] cells were treated with BSA and BSA/OA for 1 h (Fig. 2h), as previously described[1]. As shown in Fig. 2j, after 1 h, a similar percentage of nascent LDs (LiveDrop-positive, LipidTOX-negative) were produced in WT and HepG2[zDHHC11+(B)-KO] cells with BSA and OA supplementation. Most LiveDrop-positive LDs were positive for LipidTOX signals, suggesting that they could successfully mature (Fig. 2h,i). These results indicate that loss of *ZDHHC11* does not affect de novo LD formation or the accrual of neutral lipids, suggesting a role for zDHHC11 in regulating LD catabolism.

Monitoring LD catabolism is complicated by the resynthesis of TAG and de novo formation of nascent LDs during lipolysis. To mitigate this effect experimentally, we induced LD breakdown in the presence of a diacylglycerol acyltransferase 1 (DGAT1) inhibitor (DGAT1i) to prevent the resynthesis of TAG from the newly liberated fatty acids and glycerol, as previously reported[25]. Using this approach, we examined the ability of parental and HepG2[zDHHC11+(B)-KO] or MEF[shzDHHC11] cells to catabolize TAG and LDs following a shift from a rich culture medium to Hank's balanced salt solution (HBSS) containing a DGAT1i (T863). Remarkably, cells lacking zDHHC11 activity preserved their LDs under these conditions, whereas control cells displayed an ≈80% reduction (Fig. 2k,l and Extended Data Fig. 2q). Our data indicate that zDHHC11 is not required for LD growth or biogenesis but is critical for LD catabolism.

zDHHC11 is necessary for lipolysis and β-oxidation

In hepatocytes, LD catabolism is mediated by a synergistic combination of lipolysis and a selective autophagic mechanism termed lipophagy[26,27]. Mechanistically, lipolysis reduces the volume of large pre-existing LDs and facilitates the production of small nascent LDs, both of which can be targeted for lipophagic isolation and degradation[26]. To determine at which stage in the process zDHHC11 is specifically required, we used the fatty acid-conjugated fluorescent probe BODIPY 558/568 C12 (Red C12) as a surrogate to visualize the delivery of LDs to lysosomes (lipophagy) and to track the movement of liberated fatty acids from LDs to mitochondria (lipolysis and β-oxidation)[28]. Red C12 was preloaded into HepG2 and HepG2[zDHHC11+(B)-KO] cells and chased in either complete medium (CM) or nutrient-depleted medium (HBSS)
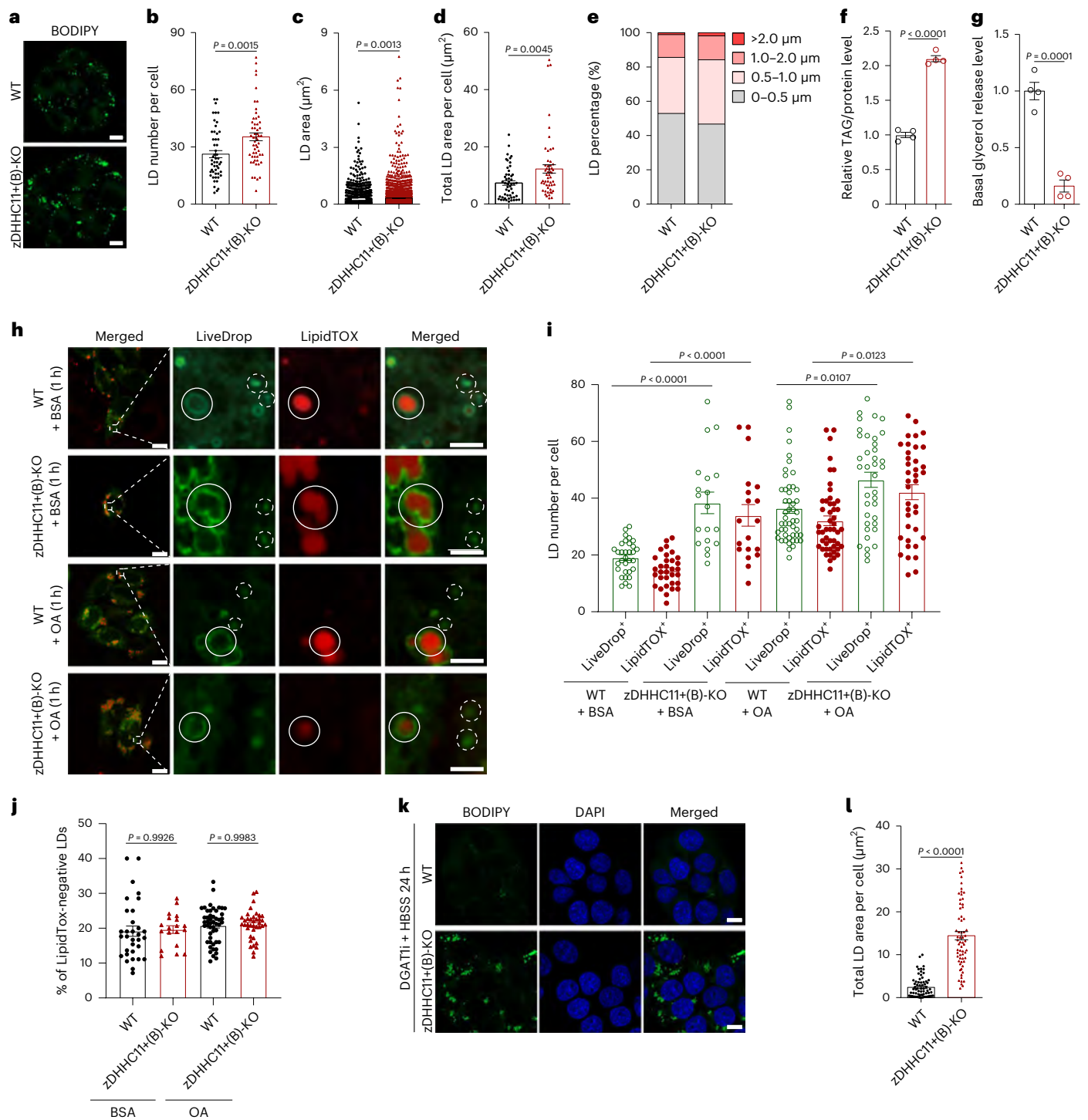
Fig. 2 | zDHHC11+(B) deficiency does not affect LD lipogenesis. a, Confocal micrographs displaying HepG2 and HepG2$^{zDHHC11+(B)-KO}$ cells, with LDs stained with BODIPY 493/503. **b–e**, Quantitative metrics derived from **a**, including the total number of LDs (**b**), the area of individual LDs (**c**), the cumulative LD area per cell (**d**) and a percentage breakdown based on LD diameters (**e**). The sample sizes across three independent experiments were $n = 51$ for HepG2 cells and $n = 55$ for HepG2$^{zDHHC11+(B)-KO}$ cells. **f**, Quantification of the total triglycerides in both HepG2 and HepG2$^{zDHHC11+(B)-KO}$ cells ($n = 4$ independent repeats). **g**, Baseline glycerol release measurements taken from both cell types ($n = 4$ independent repeats). **h**, The GFP-LiveDrop marker reveals a similar count of nascent LDs in both HepG2 and HepG2$^{zDHHC11+(B)-KO}$ cells. Green fluorescence corresponds to GFP-LiveDrop, whereas red indicates LipidTOX neutral red staining. Complete circles signify LipidTOX-positive LDs, whereas dotted circles represent LDs without LipidTOX staining. **i**, Enumeration of LDs positive for LiveDrop and

those positive for LipidTOX using the data from **h**. **j**, Percentage calculations for LDs that displayed GFP-LiveDrop signals but lacked LipidTOX staining, for both HepG2 and HepG2$^{zDHHC11+(B)-KO}$ cells. For **i** and **j**, data were from three independent experiments: $n = 32$ (HepG2 + BSA), $n = 19$ (HepG2$^{zDHHC11+(B)-KO}$ + BSA), $n = 49$ (HepG2 + OA) and $n = 38$ (HepG2$^{zDHHC11+(B)-KO}$ + OA). **k**, Confocal images of both HepG2 and HepG2$^{zDHHC11+(B)-KO}$ cells after a 24-h incubation in HBSS supplemented with a DGAT1i. LDs were visualized with BODIPY 493/503, and nuclei were marked with blue using 4′,6-diamidino-2-phenylindole (DAPI). **l**, Quantification of the total LD area per cell from images in **k**, with sample sizes over three independent experiments of $n = 71$ for HepG2 cells and $n = 65$ for HepG2$^{zDHHC11+(B)-KO}$ cells. Data from **b**, **c**, **d**, **f**, **g**, **i**, **j** and **l** are presented as mean ± s.e.m. An unpaired two-tailed Student's t test was used for data in **b**, **c**, **d**, **f**, **g** and **l**. One-way ANOVA and Tukey's post hoc tests were used for **i** and **j**. Scale bars are set at 10 μm (2 μm for insets).

for 24 h, followed by labelling with LysoTracker. Confocal microscopy of Red C12 in WT HepG2 cells under starvation conditions revealed that Red C12 was redistributed to LysoTracker-positive compartments and in LD remnants (Fig. 3a). In contrast, in starved HepG2[zDHHC11+(B)-KO] cells, Red C12 remained associated with LDs with little signal in lysosomes (LysoTracker) (Fig. 3b).

We investigated autophagy proteins important for lipophagy, including LC3B, p62, ATG5 and ATG16L1 (ref. 24). In the control medium, we observed that the relative abundance of the autophagy proteins p62 and LC3B was comparable between HepG2 and HepG2[zDHHC11+(B)-KO] cells (Extended Data Fig. 3a,b). Furthermore, there was no noticeable difference in the LC3B-I to LC3B-II ratio, suggesting that autophagy was neither blocked nor stimulated. However, we noted a threefold increase in the total PLIN3 levels in HepG2[zDHHC11+(B)-KO] cells under the same conditions (Extended Data Fig. 3a,b), which is again consistent with more LDs. We used confocal microscopy to examine PLIN3 localization and confirmed that it remained associated with LDs in various conditions. Predictably, the association of PLIN3 with LDs in HepG2 cells was reduced following starvation. This response was not detected in HepG2[zDHHC11+(B)-KO] cells (Extended Data Fig. 3c,d). These results suggest a specific disruption of lipophagy, rather than general autophagy, in HepG2[zDHHC11+(B)-KO] cells. This notion is supported by the observation that zDHHC11 overexpression reduced LDs in ATG5-null cells (Extended Data Fig. 3e–h), indicating that this effect is independent of autophagy.

Next, to determine whether zDHHC11 is required for lipolysis and the release of fatty acids for β-oxidation, cells treated as above were labelled with a mitochondrial marker (MitoTracker) and visualized by confocal microscopy (Fig. 3c,d). Quantitative analysis of Red C12-stained LDs after the chase period in CM revealed an increase in the LD size and total area in the cell for HepG2[zDHHC11+(B)-KO] cells compared with control HepG2 cells (Fig. 3e,f), consistent with our findings using BODIPY (Fig. 2d,e). Remarkably, HepG2[zDHHC11+(B)-KO] cells incubated in a nutrient-depleted medium (HBSS) showed a modest redistribution of Red C12 from LDs into mitochondria, in contrast to the WT cells (Fig. 3d,g). Starved WT cells displayed a ≈60% reduction in the total LD area per cell (Fig. 3c,e), whereas HepG2[zDHHC11+(B)-KO] cells showed a ≈30% decrease (Fig. 3d,e), indicating impaired lipolysis in HepG2[zDHHC11+(B)-KO] cells. Given the observed general impairment in lipolysis, we wondered how mitochondrial β-oxidation is affected. To assess β-oxidation, we measured the mitochondrial oxygen consumption rate (OCR) in both CM and starvation conditions. In line with the inability of HepG2[zDHHC11+(B)-KO] cells to mobilize fatty acids even under normal conditions, we observed that the mitochondrial OCR was significantly lower than that in WT cells in both CM (Fig. 3h) and serum-starved conditions (Fig. 3i). To confirm the role of zDHHC11 in lipolysis, we treated WT and KO cells with the adenylyl cyclase activator forskolin (FSK) (10 μM, 24 h) to increase cAMP levels, activate PKA and simulate lipolysis[26,29]. As expected, FSK treatment caused a significant decrease in the total LD area per cell for WT cells but not HepG2[zDHHC11+(B)-KO] cells (Fig. 3j,k). Together, these data suggest that zDHHC11+(B) loss disrupts both the lipophagy and lipolysis pathways of LD catabolism, limiting fatty acid mobilization for β-oxidation. This multimodal impairment

causes lipid accumulation, indicating that zDHHC11+(B) is required for cellular lipolytic responses by potentially engaging cytoplasmic neutral lipases.

zDHHC11 interacts with and S-acylates ATGL

Previous studies have illustrated that, akin to zDHHC11 depletion, loss of ATGL results in a marked enlargement in LD size and a significant reduction in fatty acid transit to mitochondria[28]. Overexpressing WT ATGL, which primarily localizes to the ER before concentrating on LDs[10], brings about a notable decrease in LD size (Extended Data Fig. 4a). Observing the importance of zDHHC11+(B) for neutral lipolysis and considering the numerous metabolic factors and binding partners that influence ATGL activity, we examined several of these under CM conditions to comprehend the ramifications of zDHHC11 loss. Intriguingly, in contrast to WT cell lysates, phosphorylated S6 kinase (p-S6K), a substrate of the mammalian target of rapamycin (mTOR), was elevated in zDHHC11-KO cell lysates, implying activation of mTOR complex 1 (mTORC1) signalling and protein synthesis (Fig. 4a and Extended Data Fig. 4b). We further observed no significant difference for p-AMPK (Fig. 4a and Extended Data Fig. 4b). As can be seen in Fig. 4a, there was no difference for total ATGL, HSL and the ATGL coactivator CGI-58. However, there was a significant difference for p-ATGL[15,16], p-HSL (Ser565)[30] and p-HSL (Ser660)[30]. These results paradoxically suggest that ATGL was activated and HSL was inhibited in HepG2[zDHHC11+(B)-KO] cells compared with HepG2 cells (Fig. 4a and Extended Data Fig. 4b)[5,31]. Collectively, these changes indicate that loss of zDHHC11 induces a dysfunctional metabolic state characterized by aberrant lipolysis regulation, given the increased ATGL/HSL phosphorylation without actual lipolysis, and augments anabolism through mTORC1-mediated protein synthesis.

Given the preceding observations, we speculated that the most direct mechanism through which zDHHC11 could modulate lipolysis is by regulating ATGL, the pivotal lipase that catalyses the rate-limiting step in LD degradation. We hypothesized that zDHHC11 could affect ATGL in two ways: zDHHC11 could influence the targeting of ATGL to the LDs or it could influence the catalytic activity of ATGL, directly or indirectly. In support of this hypothesis, previous research has shown that, like zDHHC11 depletion, ATGL loss leads to a significant increase in LD size and drastically reduced trafficking of fatty acids to mitochondria from LDs[28]. Furthermore, overexpression of WT ATGL, which initially localizes to the ER and then concentrates on LDs[10], causes a marked decrease in LD size (Extended Data Fig. 4a). These findings were correspondingly phenocopied in zDHHC11 overexpression (Fig. 1b), depletion (Extended Data Fig. 2e) and KO (Fig. 2a) experiments. As the total levels of ATGL were unaffected (Fig. 4a and Extended Data Fig. 4b), we wondered whether the zDHHC11-mediated LD phenotype could be linked to altered ATGL subcellular localization in WT HepG2 and HepG2[zDHHC11+(B)-KO] cells. As seen in Fig. 4b,c, and although HepG2 cells lacking zDHHC11+(B) do not retain the ability to catabolize LDs in response to starvation (Fig. 3b), the ATGL subcellular localization was similar in WT HepG2 and HepG2[zDHHC11+(B)-KO] cells for each metabolic scenario. Additionally, CGI-58 subcellular localization appeared normal in KO cells following overexpression (Extended Data Fig. 4c).

Fig. 3 | zDHHC11 is necessary for LD catabolism. a,b, Confocal micrographs of HepG2 (**a**) and HepG2[zDHHC11+(B)-KO] (**b**) cells after pulsing with Red C12 and subsequent labelling of lysosomes with LysoTracker. **c,d**, HepG2 (**c**) and HepG2[zDHHC11+(B)-KO] (**d**) cells were pulsed with Red C12 overnight, followed by a wash and a 1-h incubation in CM, facilitating Red C12 accumulation in LDs. A subsequent chase was conducted in either CM or HBSS for 24 h. During this process, mitochondria were marked using MitoTracker. **e–g**, Quantification of the following metrics from the images in **a–d**: total LD area per cell (**e**), percentage distribution of LDs by diameter (**f**) and mean fluorescence intensity of Red C12 (**g**). Data were from three independent experiments: in CM, n = 28 (HepG2) and n = 32 (HepG2[zDHHC11+(B)-KO]); in 24-h HBSS, n = 35 (HepG2) and n = 33 (HepG2[zDHHC11+(B)-KO]). **h,i**, OCRs of HepG2 and HepG2[zDHHC11+(B)-KO] cells measured after incubation in CM

(**h**) or HBSS (**i**) for 24 h. During these measurements, oligomycin, FCCP and the combination of rotenone and antimycin A (AA) were introduced at specified intervals. The experiment was independently repeated five times for **h** and four times for **i**. **j**, HepG2 and HepG2[zDHHC11+(B)-KO] cells were treated with either DMSO or FSK (10 μM) in CM over 24 h. LDs in these cells were highlighted using LipidTOX Red. **k**, Quantification of the total LD area per cell using images from **j**. The sample distributions over three independent experiments were as follows: n = 71 (HepG2 + DMSO), n = 76 (HepG2 + FSK), n = 60 (HepG2[zDHHC11+(B)-KO] + DMSO) and n = 82 (HepG2[zDHHC11+(B)-KO] + FSK). Data from **e**, **g**, **h**, **i** and **k** are denoted as mean ± s.e.m. One-way ANOVA and Tukey's post hoc tests were used for **e**, **h**, **i** and **k**, whereas Student's t test was used for data in **g**. All images have a scale bar of 10 μm.

Given the discrepancy between the apparent ATGL phosphorylation, accumulation of LDs and impaired lipolysis in HepG2$^{zDHHC11+(B)-KO}$ cells, we examined the LD-associated pools of various ATGL regulators, including ELMOD2, G0S2, acyl-CoA synthetase long-chain family member 1 (ACSL1) and hypoxia-inducible LD-associated protein (HILPDA). As supplementation with OA and palmitate to increase LD

content results in a variety of cellular responses that may confound the analysis[32–35], we chose to overexpress Flag-tagged LiveDrop and immunocapture LiveDrop-positive LDs with M2 anti-Flag beads (Extended Data Fig. 4d,e). In contrast to the LD fraction from WT HepG2 cells (Extended Data Fig. 4d,e), G0S2 was significantly decreased in HepG2$^{zDHHC11+(B)-KO}$ cells, whereas the ACSL1 fraction was significantly
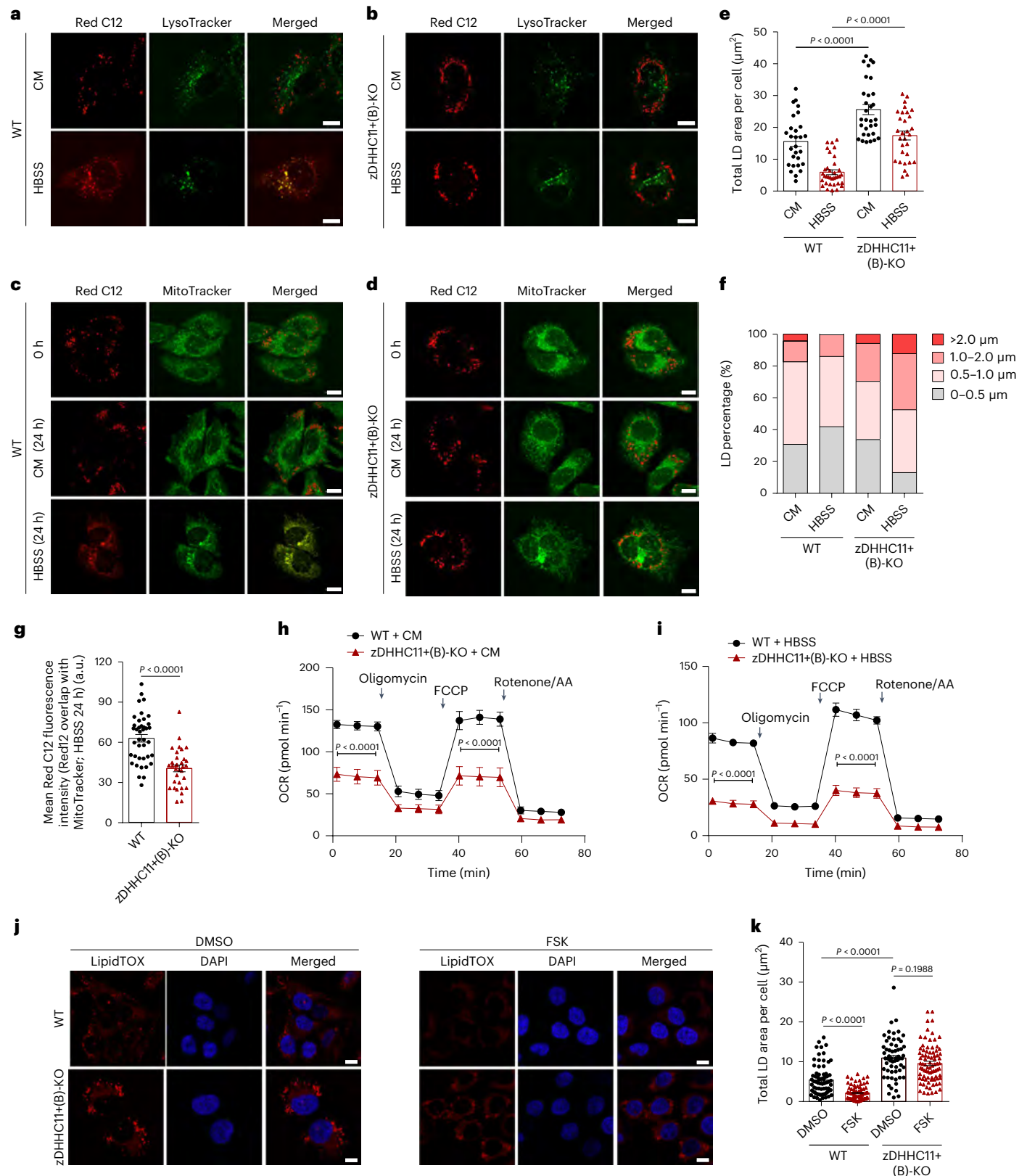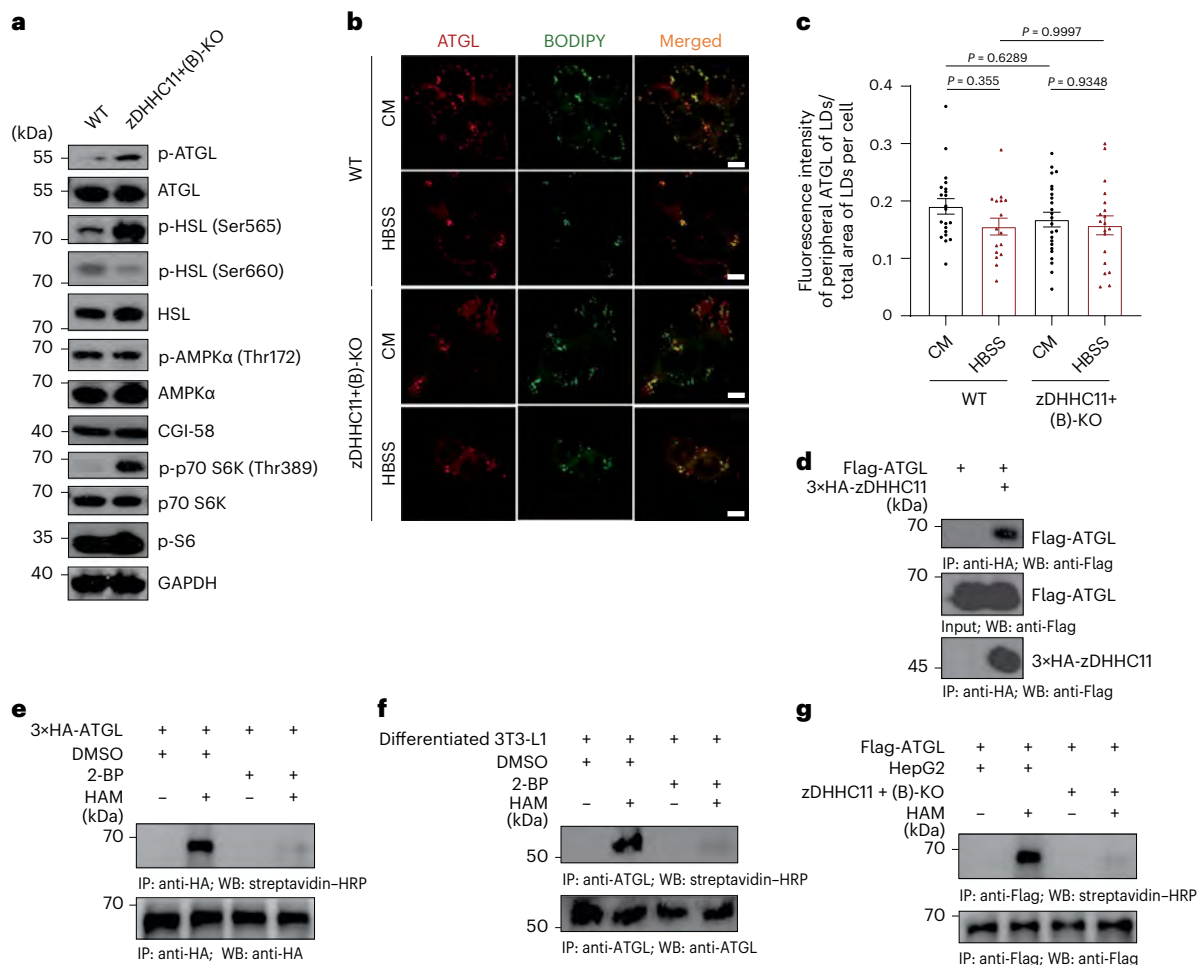
Fig. 4 | ATGL is S-acylated by zDHHC11. a, Representative immunoblot analyses of HepG2 and HepG2^zDHHC11+(B)-KO cells for the following proteins and phosphorylation sites: ATGL, ATGL phosphorylation, HSL, HSL Ser565 phosphorylation, HSL Ser660 phosphorylation, AMPK, AMPKα Thr172 phosphorylation, CGI-58, p70 S6K, p70 S6K Thr389 phosphorylation, p-S6 and GAPDH (*n* = 3 independent repeats). **b**, Confocal images displaying endogenous ATGL proteins in HepG2 and HepG2^zDHHC11+(B)-KO cells treated with CM and HBSS. LDs were visualized using BODIPY 493/503 staining. Data were from three independent experiments: in CM, *n* = 21 (HepG2) and *n* = 24 (HepG2^zDHHC11+(B)-KO); in 24-h HBSS, *n* = 16 (HepG2) and *n* = 19 (HepG2^zDHHC11+(B)-KO). **c**, Quantitative analysis of ATGL fluorescence intensity on LDs, normalized to the total LD area in cells shown in **b**. **d**, Co-IP of 3×HA-zDHHC11 and Flag-ATGL from cotransfected HEK293T cells (*n* = 2 independent repeats). **e**, Analysis of S-acylation levels of 3×HA-ATGL in HEK293T cells treated with or without HAM, both in the absence or presence of 2-BP (*n* = 3 independent repeats). **f**, S-acylation levels of endogenous ATGL assessed in differentiated 3T3-L1 cells treated with HAM or 2-BP as in **e** (*n* = 2 independent repeats). **g**, S-acylation levels of Flag-tagged ATGL in HepG2 and HepG2^zDHHC11+(B)-KO cells after HAM treatment (*n* = 3 independent repeats). Data in **c** are presented as mean ± s.e.m., with analysis conducted using one-way ANOVA and Tukey's post hoc tests. All images have a scale bar of 10 μm.

increased in HepG2^zDHHC11+(B)-KO cells. Interestingly, ACSL1 also showed a significant increase in the total HepG2^zDHHC11+(B)-KO cell lysates. The decreased LD association of the ATGL inhibitor G0S2 could increase ATGL activity and lipolysis in HepG2^zDHHC11+(B)-KO cells. However, we observed impaired lipolysis in zDHHC11-KO cells, contrary to this prediction. Additionally, the increased association of ACSL1 with LDs in HepG2^zDHHC11+(B)-KO cells should promote the mobilization of fatty acids to support sustained lipolysis. Again, we did not see evidence of enhanced lipolysis in zDHHC11-KO cells. Collectively, these observations indicate that TAG lipolysis is disrupted in HepG2^zDHHC11+(B)-KO cells despite changes in G0S2 and ACSL1 that would theoretically increase ATGL activity and lipolysis.

Therefore, we hypothesized that zDHHC11 might influence ATGL directly via protein–protein interaction. To test this, we immunoprecipitated cells expressing Flag-tagged ATGL and 3×HA-zDHHC11, and as a control, cells expressing Flag-tagged ATGL and 3×HA-zDHHC16, using a monoclonal anti-haemagglutinin antibody. As shown in Fig. 4d, 3×HA-zDHHC11 was found in the captured proteins, but the control 3×HA-zDHHC16 was not (see Extended Data Fig. 4f). These data support the conclusion that zDHHC11 regulates LD lipolysis by interacting with ATGL. Given that zDHHC11 is a protein acyltransferase and having established that zDHHC11 interacts with ATGL, we hypothesized that ATGL might be S-palmitoylated/-acylated by zDHHC11. To test this directly, we used the acyl–biotin exchange (ABE) assay, which consists of a series of biochemical reactions involving the exchange of the fatty acids attached to cysteine residues for biotin, which can then be detected by streptavidin[36]. Using the ABE assay, we found that ectopically expressed 3×HA-ATGL in HEK293 cells, as well as endogenous ATGL from HepG2 and differentiated 3T3-L1 cells, were S-acylated (Fig. 4e,f and Extended Data Fig. 4g,h). The dependency on hydroxylamine (HAM) in the ABE assay demonstrated that ATGL is acylated through a thioester linkage, consistent with the function of zDHHC enzymes. Furthermore, ATGL S-acylation levels were attenuated by the nonselective zDHHC inhibitor 2-bromopalmitate (2-BP) (Fig. 4e,f and Extended Data Fig. 4g,h). Importantly, the S-acylation of ATGL was largely abolished in HepG2^zDHHC11+(B)-KO cells (Fig. 4g and Extended Data Fig. 4i). Taken together, these results indicate that ATGL is S-acylated and zDHHC11+(B) is the primary protein acyltransferase for ATGL.

ATGL is S-acylated on multiple cysteine residues

We next aimed to identify specific sites of ATGL S-acylation using scanning mutagenesis combined with confocal microscopy and ABE assays. Given that overexpressed ATGL eliminates LDs, we determined whether overexpression of the individual cysteine mutants phenocopy the WT or catalytically inactive S47A ATGL (Extended Data Fig. 5a). As shown in Extended Data Fig. 5a, among all cysteine mutants tested (C15S, C28S, C61S, C144S, C152S, C194S, C238S, C312S, C374S, C412S, C439S and C449S), only the C15S mutant preserved LD abundance and remained associated with LDs, similar to the catalytically inactive ATGL[S47A]. Moreover, ABE analysis identified Cys15 as an S-acylation site (Extended Data Fig. 5b,c).

We also performed ABE assays on C61S, C144S, C152S, C238S, C312S, C374S and C412S (Extended Data Fig. 5b–k). Notably, Cys144 was also found to be S-acylated (Extended Data Fig. 5d,e). Interestingly, the overexpression of the ATGL[C144S] mutant protein showed a similar effect to that of WT ATGL, leading to the disappearance of LDs, as shown in Extended Data Fig. 5a. This observation suggests that the S-acylation of Cys144 is not essential for its function, and overexpression compensates for any loss in function in cells. To understand how S-acylation at Cys144 might affect ATGL, we should note that Cys144 is adjacent to the LC3-interacting region (LIR) motif, 144-CSTFIPVY-151 (ref. 37). The LIR motif is known to mediate the binding of ATGL to LC3 to facilitate the lipophagic degradation of LDs and is also required for ATGL to target LDs[37]. Indeed, we found that mutating Phe147 in the LIR led to cytosolic accumulation (Extended Data Fig. 5a) and diminished S-acylation (Extended Data Fig. 5f,g), indicating the importance of the LIR motif for ATGL localization and S-acylation. Currently, without high-resolution structural information, we cannot predict how S-acylation at Cys144 and the LIR motif influence the subcellular targeting, activity and S-acylation of ATGL. However, given that C144S is still able to eliminate LDs, it can be inferred that the S-acylation of this site is not essential for activity in cells, contrary to Cys15.

ATGL Cys15 S-acylation is necessary for ATGL lipase activity

As the C144S mutant eliminated LDs, and this is not the phenotype of the zDHHC11+(B)-KO cells, we chose to focus on the role of Cys15 S-acylation. To assess the role of this post-translational modification, we generated a HepG2 cell line that overexpresses an shRNA targeting the 3′ untranslated region of ATGL (Extended Data Fig. 6a,b). We next performed rescue experiments using this cell line by overexpressing shRNA-resistant mCherry-tagged ATGL constructs, ATGL, ATGL[C15S] and catalytically inactive ATGL[S47A], and assessed LDs using LipidTOX. As shown in Extended Data Fig. 6a, overexpression of mCherry-ATGL abolished LDs. However, mCherry-ATGL[C15S] and mCherry-ATGL[S47A] proteins, despite their localization to LDs, had no impact on LD size or abundance compared with that in nontransfected neighbouring cells (Extended Data Fig. 6a). We next complemented these results using a knockin HepG2 cell line (HepG2[ATGL.C15S]) generated using

CRISPR/Cas9 and validated by sequencing (Extended Data Fig. 6c). The endogenous expression of ATGL[C15S] was confirmed by immunofluorescence (Extended Data Fig. 6d) and immunoblotting using antibodies to ATGL (Fig. 5a and Extended Data Fig. 6e). Consistent with our transient transfection results (Extended Data Fig. 5b,c), the C15S mutant also displayed a reduction in the degree of S-acylation using ABE (Fig. 5b and Extended Data Fig. 6f) despite the abundance of zDHHC11 being similar between the genotypes (Extended Data Fig. 6g,h). Of note, the residual S-acylation can be attributed to the other site, Cys144, as identified above (Extended Data Fig. 5d,e). Importantly, TAG content measurement and BODIPY staining indicated an increase in the LD number and size in HepG2[ATGL.C15S] cells (Fig. 5c,d), and this phenotype could be reversed by overexpressing WT ATGL (Fig. 5e). Thus, the results obtained with the ATGL mutant that is nonmodifiable on Cys15 were harmonious to those obtained for HepG2[zDHHC11+(B)-KO] cells.

To clarify the role of the S-acylation-deficient mutation ATGL[C15S] in LD homoeostasis, we examined specific pathways affecting LDs using total lysates grown in CM. We observed an increase in p-S6K, p-ATGL and p-HSL (Ser565) and a decrease in p-HSL (Ser660) (Fig. 5a and Extended Data Fig. 6e). Additionally, HepG2[ATGL.C15S] cells displayed a significant increase in the p-AMPK (Thr172) and PLIN3 protein levels (Fig. 5a,f,g and Extended Data Fig. 6e). Notably, the association of PLIN3 with LDs in HepG2[zDHHC11+(B)-KO] cells showed congruence with that in HepG2[ATGL.C15S] cells when compared with WT cells in both CM and starvation conditions (Fig. 5f,g). Further analysis of the immunoblots indicated elevated phosphorylation of ATGL and HSL Ser565 in the C15S mutant, although ATGL enzymatic activity was impaired. The changes to p-HSL Ser660 and the increase in p-AMPK suggest dysregulated signalling and metabolic stress, respectively. We also observed increased p-p70 S6K, implying upregulated mTORC1 activity and protein synthesis. Finally, the accumulation of PLIN3 correlated with an increase in LD content. Together, these data are consistent with the ATGL[C15S] mutation leading to dysfunctional lipolysis, metabolic abnormalities and lipid accumulation. This conclusion is bolstered by the immunoblot results following the overexpression of Flag-tagged LiveDrop and the subsequent immunoprecipitation (IP) of LiveDrop-positive LDs using M2 Flag beads, as shown in Extended Data Fig. 4d. In line with the findings shown in Extended Data Fig. 4d, the isolated LDs from HepG2[ATGL.C15S] cells (Extended Data Fig. 6i,j) exhibited a significant reduction in G0S2 levels compared with those from WT HepG2 cells, whereas the ACSL1 level was significantly elevated. These findings imply that neutral lipolysis is impaired in HepG2[ATGL.C15S] cells despite alterations in G0S2 and ACSL1 that would theoretically enhance ATGL-mediated lipolysis. Again, the cellular state of cells with the ATGL[C15S] mutation mirrors that of zDHHC11-KO cells (Fig. 4a and Extended Data Fig. 4b), consistent with the concept that inhibited ATGL is due to loss of S-acylation at the Cys15 position.

To explore the functional role of this S-acylation site further, we used a range of assays as we have done for HepG2[zDHHC11+(B)-KO] cells,

Fig. 5 | ATGL Cys15 palmitoylation is necessary for ATGL lipase activity.
a, Immunoblots for the indicated proteins in HepG2 and HepG2[ATGL.C15S] cells ($n = 3$ independent repeats). **b**, S-acylation levels of endogenous ATGL in both HepG2 and HepG2[ATGL.C15S] cells ($n = 2$ independent repeats). **c,d**, Confocal visualization of LDs stained with BODIPY 493/503 (**c**) and total TAGs (**d**) in HepG2 and HepG2[ATGL.C15S] cells ($n = 4$ independent repeats). **e**, Fluorescence micrographs of HepG2[ATGL.C15S] cells expressing mCherry-ATGL or mCherry-ATGL[C15S], with LDs stained using BODIPY 493/503. **f**, Confocal visualization of endogenous PLIN3 protein in HepG2 and HepG2[ATGL.C15S] cells in CM and HBSS, with LDs stained using BODIPY 493/503. **g**, PLIN3 fluorescence intensity at the LD periphery, normalized to the total LD area in the cells shown in **f**. Data were from three independent experiments: CM cells, $n = 24$ (HepG2), $n = 17$ (HepG2[ATGL.C15S]); in 24-h HBSS, $n = 18$ (HepG2), $n = 18$ (HepG2[ATGL.C15S]). **h,i**, OCR measurements in HepG2 and HepG2[ATGL.C15S] cells after 24 h in CM (**h**) or HBSS (**i**), with oligomycin, FCCP and rotenone/antimycin A added at intervals. The experiments were independently repeated five times for

h and four times for **i**. **j**, Confocal images of HepG2 and HepG2[ATGL.C15S] cells in HBSS for 24 h with a DGAT1i, stained using BODIPY 493/503 and DAPI. **k**, In vitro lipase activity assay for the indicated ATGL WT and mutant proteins using radiolabel−[9,10(N)-3H]glycerol trioleate ($n = 3$ independent repeats). FA, fatty acid. **l,n**, Oil Red O staining of liver sections from mice fed a normal diet (**l**) or an HFD (**n**). **m,o**, Total triglycerides in liver samples from mice fed a normal diet (**m**) or an HFD (**o**). Sample sizes: for mice on a normal diet (**m**), $n = 7$ (transduced with shmATGL[endo]::mATGL[exo]) and $n = 5$ (transduced with AAV-shmATGL[endo]::mATGL[C15S][exo]); for mice fed an HFD (**o**), $n = 7$ (transduced with shmATGL[endo]::mATGL[exo]) and $n = 9$ (transduced with AAV-shmATGL[endo]::mATGL[C15S][exo]). **p**, Immunoblot analysis of the indicated proteins in liver samples from mice fed a normal diet or an HFD. For **d**, **g**, **h**, **i**, **k**, **m** and **o**, values are presented as mean ± s.e.m. An unpaired two-tailed Student's t test was applied to data in **d**, **n** and **p**. One-way ANOVA and Tukey's post hoc tests were applied to data in **g**, **h**, **i** and **k**. All images have a scale bar of 10 μm.
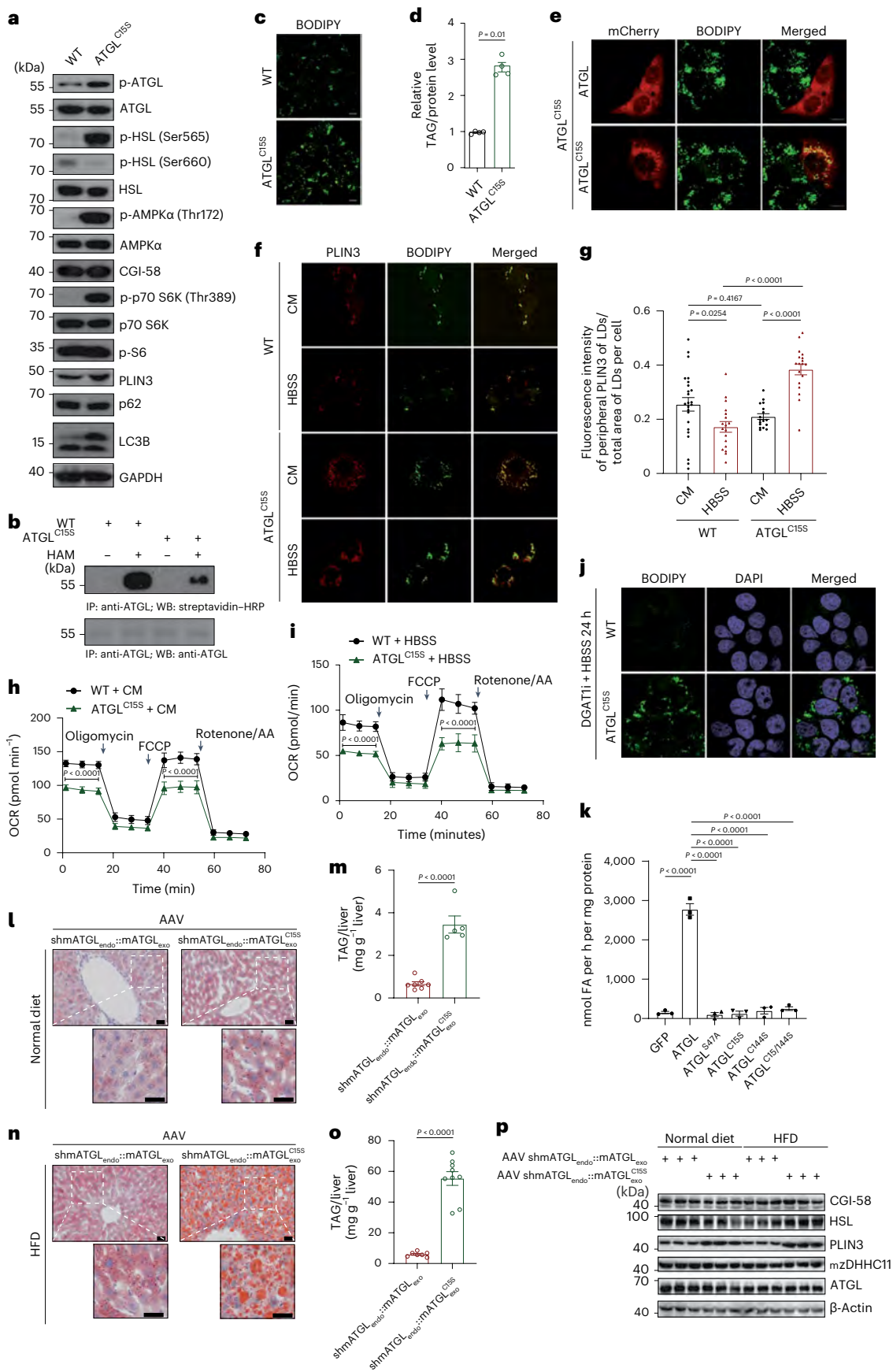
including measuring the mitochondrial OCR in both CM (Fig. 5h) and serum-starved (Fig. 5i) conditions, Red C12 pulse–chase (Extended Data Fig. 6k–n), and DGAT1i-dependent LD formation under nutrient starvation (Fig. 5j). Importantly, all results were analogous to those obtained for HepG2[zDHHC11+(B)-KO] cells, further reinforcing the enzyme–substrate relationship between zDHHC11 and ATGL and the importance of post-translational modification. As in the case of HepG2[zDHHC11+(B)-KO] cells, the observed reduced lipolytic activity of mutant ATGL[C15S] in HepG2[ATGL.C15S] cells could not be attributed to changes in the abundance or localization of its coactivator protein, CGI-58 (Fig. 5a and Extended Data Fig. 6e,o).

In line with the observations in HepG2[zDHHC11+(B)-KO] cells (Fig. 3b), in HepG2[ATGL.C15S] cells, starvation failed to mobilize Red C12 to LysoTracker-positive compartments (Extended Data Fig. 6l). These results collectively suggest that while acylation of ATGL at Cys15 does not influence its localization, it may affect the enzyme's catalytic activity. To investigate this, we used two distinct assays: a radiolabel-based assay using [9,10(N)-³H]triolein as a tracer and a fluorescence-based assay with EnzCheck lipase substrate to assess enzymatic activity. Lysates from HepG2 cells transiently overexpressing GFP, GFP-ATGL, GFP-ATGL[S47S], GFP-ATGL[C15S], GFP-ATGL[C144S] and GFP-ATGL[C15/144S] were incubated with [9,10(N)-³H]triolein complexed as phospholipid–triolein emulsions, as previously described by Schweiger et al.[38]. Significantly, cell lysates expressing GFP-ATGL released ≈20-fold more radiolabelled free fatty acids compared with controls (Fig. 5k). In contrast, lysates from cells expressing GFP, GFP-ATGL[C15S], GFP-ATGL[C144S] and GFP-ATGL[C15/144S] displayed similar activities as the catalytically inactive GFP-ATGL[S47S] protein (Fig. 5k). This suggests that ATGL Cys15 acylation is critical for lipase activity, as shown by its decreased activity despite associating with LDs (Extended Data Fig. 5a). Similar results using fluorescence-based assays were observed for ATGL[C15S] when lysates from cells expressing GFP, GFP-ATGL and GFP-ATGL[C15S] were incubated with micelles containing quenched EnzCheck as a substrate. We noted a significant release of BODIPY by cells expressing GFP-ATGL compared with controls, whereas cells expressing GFP-ATGL[C15S] did not demonstrate such activity (Extended Data Fig. 7a).

To corroborate our findings in vivo, we generated AAVs capable of concurrently knocking down endogenous mouse ATGL (mATGL) in the liver and overexpressing either WT mATGL or mATGL[C15S], as demonstrated in Extended Data Fig. 7b–e. We verified the effectiveness of these AAVs, and Extended Data Fig. 7b–e shows that overexpression of WT mATGL in mouse livers led to a decrease in LDs and TAG content. This contrasted with mice expressing the mATGL[C15S] mutant, regardless of whether they were fed a standard chow (Fig. 5l,m) or an HFD (Fig. 5n,o). Remarkably, paralleling the observations in Figs. 3a and 5g, there was a significant increase in PLIN3 expression in livers expressing the S-acylation-deficient ATGL (mATGL[C15S]), as compared with those expressing the WT mATGL (Fig. 5p and Extended Data Fig. 7f). However, HSL, CGI-58 and ATGL levels remained unchanged, irrespective of dietary variations. Collectively, these findings underscore that S-acylation of ATGL at the Cys15 position is essential for its enzymatic activity within the cell.

Discussion

Herein, we showed that the post-translational S-acylation of ATGL at Cys15 by the zDHHC11+(B) acyltransferase has a crucial role in LD catabolism by enhancing the catalytic activity of ATGL. Given that overexpression of zDHHC11 substantially enhances the activity of ATGL, it can be inferred that, at the steady state, only a fraction of the total cellular pool of ATGL is S-acylated and maximally active. Our study focused on hepatocytes, but a previous proteomic study using adipocytes identified ATGL as a potentially S-acylated protein, although the sites and, more importantly, the role of the modification were not examined[39]. Given our results, we suspect that this modification will be required in all tissues with robust ATGL activity. Adding

palmitate or another fatty acid to Cys15 could be required for optimal enzymatic activity by inducing a conformational change in the catalytic site or promoting the interaction of the catalytic site with the limiting membrane of the LDs. The biological function of Cys144 needs to be clarified as overexpression of ATGL[C144S] eliminates LDs (Extended Data Fig. 5a), yet it has minimal activity in a cell-free assay (Fig. 5k). One possibility is that Cys144, its S-acylation and the LIR motif may have more subtle structural roles in other aspects of ATGL regulation that are not truly essential for catalysis. Ultimately, when high-resolution structures become available for ATGL and relevant mutants, it should be possible to theorize and test the structural basis of our observations.

Overexpression of zDHHC11 significantly reduced total LDs in cells (HepG2, Huh7 and AML12) and in vivo (mice fed a normal diet or an HFD). Conversely, ZDHHC11 knockdown and KO increased the total LD content, which is refractory to depletion following nutrient deprivation or cAMP-induced lipolysis independent of the presence of the ATGL activator CGI-58. The recent gene duplication of ZDHHC11 may help explain why loss-of-function variants are not identified in unbiased screens. However, a pilot genome-wide association study indicated that ZDHHC11 is hypermethylated and downregulated in liver biopsy specimens from patients with type 2 diabetes[40]. The accumulation of LDs in hepatocytes is a hallmark of nonalcoholic fatty liver disease and hepatocellular carcinoma (HCC)[7–9]. Thus, a loss or reduction in ATGL S-acylation may contribute to this disease.

Overexpression of ZDHHC11 abolished LDs in control and ATG5-silenced cells. This demonstrates that rampant ATGL activity can eliminate LDs without the requirement for the canonical autophagy/lipophagy pathway (Extended Data Fig. 3e–h). Furthermore, cells lacking zDHHC11 activity did not display overt autophagy induction or inhibition (Extended Data Fig. 3a,b). This suggests that additional protein targets of zDHHC11 are not critical for autophagy, and maximal ATGL activity is not absolutely required to support autophagy. However, it is important to highlight that ATGL facilitates lipophagy through a few nonmutually exclusive ways. First, ATGL contains a LIR domain that can physically link ATGL to LC3 on isolation membranes[37]. Second, monounsaturated fatty acids released from ATGL-mediated TAG hydrolysis can be carried by PLIN5 to the nucleus, where the fatty acid can allosterically activate sirtuin 1 (SIRT1), thereby enhancing the activities of peroxisome proliferator-activated receptor-γ (PPARγ) coactivator 1α (PGC-1α) and PPARα to promote autophagy, mitochondrial biogenesis and oxidative metabolism[41–43]. Third, large organelles, such as LDs or elongated and tubular networks of mitochondria, are spared from autophagic consumption partly due to the physical challenge of engulfing these structures with an isolation membrane[26,44]. In the case of LDs, ATGL activity can produce smaller LDs for consumption. Given that mutations in the LIR domain displace ATGL from LDs and decrease the S-acylation of ATGL (Extended Data Fig. 5a–g), it is challenging to conclude the precise role of the LIR domain. However, it is clear that simply the presence of a catalytically impaired ATGL[C15S] is not sufficient to support the elimination of LDs following starvation. Thus, we propose a model whereby either continual low-level or an initial burst of ATGL activity results in the generation of monounsaturated fatty acids and the release of PLIN2, PLIN3 and PLIN5 from the LDs that then support further activation of ATGL and concomitant enhancement of SIRT1 activity. This positive feedback activation of ATGL would generate sufficiently small LDs, either through the reduction in the size of pre-existing LDs or the generation of nascent LDs; lipophagy could complete their catabolism.

Our findings expand the complex regulation of ATGL that also includes phosphorylation in response to metabolic cues (that is, AMPK, PKA)[15,16], protein–protein interactions (that is, CGI-58, G0S2)[13,14] and competitive inhibition by long-chain acyl-CoA[33]. ATGL is a known phosphoprotein[11] whose phosphorylation supports both LD recruitment[45] and lipase activity[5,15]. S-palmitoylation has been shown to influence the

phosphorylation status of other proteins in several ways, including altering their localization (for example, LIM kinase 1 (ref. 46), signal transducer and activator of transcription 3 (ref. 47)), stability (for example, Fas receptor[48]) and accessibility of phosphorylation sites (for example, epidermal growth factor receptor[49]). However, our findings demonstrate that zDHHC11 function and ATGL Cys15 acylation regulate the activity of ATGL independent of phosphorylation (Fig. 5a and Extended Data Fig. 6e), which is comparable to phosphatidylinositol 4-kinase 2α (PI4KIIα). PI4KIIα phosphorylation by glycogen synthase kinase 3β[50] directs vesicular trafficking to lysosomes, whereas the S-palmitoylation of the cysteine-rich motif, CCPCC, located within the catalytic domains of PI4KIIα, is required for the localized production of phosphatidylinositol 4-phosphate[51]. Other examples of S-palmitoylation altering enzyme activity include the activation of nitric oxide synthase 2 (ref. 52) and inhibitory carbamoyl-phosphate synthase 1 (ref. 53). Given that 10–20% of the proteome has been reported to be S-acylated, it is reasonable to hypothesize that this post-translational modification may regulate the enzymatic activity of many proteins.

Dysregulation of lipolysis and lipid homoeostasis contributes to several metabolic disorders, including fatty liver diseases and diabetes[7–9]. For instance, ATGL-KO mice develop severe hepatic steatosis[54]. In support of this concept, we observed a reduction in *ZDHHC11* expression in human HCC samples. Thus, modulating zDHHC11–ATGL activity may offer therapeutic potential for treating such diseases. Our findings uncover a previously unrecognized mechanism for regulating ATGL activity and LD metabolism, which could pave the way for strategies targeting zDHHC11-mediated ATGL S-acylation to correct pathological lipid accumulation.

Methods

Reagents

DMEM (L110KJ) was purchased from Shanghai BasalMedia Technology. From Gibco, we acquired FBS (10270-106). Polyethylenimine (PEI) (23966-2) was sourced from Polysciences. Thermo Fisher supplied several products, including Lipofectamine 2000 (11668-019), Lipofectamine 3000 (L3000-015), GeneJET RNA purification kit (K0732), SuperScript VILO cDNA kit (11754250), HCS LipidTOX Red neutral lipid (H34476), HCS LipidTOX Deep Red neutral lipid (H34477), BODIPY 558/568 C12 (D3835), BODIPY 493/503 (D3922), SuperSignal West Pico PLUS (43580) and LysoTracker Deep Red (L12492). T863 (DGAT1i, HY-32219) was procured from MedChemExpress. Electron Microscopy Sciences provided paraformaldehyde (PFA) (15710). Saponin (EA21BA005) was bought from BBI Life Sciences. Bimake was the source of protease inhibitors (B14001), phosphatase inhibitors A and B (B15001-A and B15001-B), and anti-Flag beads (B23102). Products from Millipore Sigma included 2-bromohexadecanoic acid (21604), N-ethylmaleimide (NEM) (04260), HAM solution (467804), puromycin (P7255) and collagenase from *Clostridium histolyticum* (C0130). 5-Bromo-4-chloro-3′-indolyphosphate (BCIP; A610072-0100) and nitro blue tetrazolium (NBT; A100329) were procured from Sangon Biotech. From Vazyme Biotech, we obtained EZLink BMCC-biotin (21900), 2× Phanta HS Master Mix (VP512-01) and ClonExpress MultiS One Step Cloning Kit (C113-02). Abcam provided the lipid extraction kit (chloroform-free) (ab211044) and the lipolysis assay kit (ab185433). The EnzyChrom triglyceride assay kit (ETGA-200) was from Bioassay Systems. Agilent's supplies included Seahorse XF calibrant solution 500 ml (100840-000), Seahorse XF96 V3 PS culture microplates (101085-004), Xfe96 FluxPak Mini (Xfe96) (102601-100) and XF DMEM base medium, pH 7.4 (103575-100). Sigma was the source of 3-isobutyl-1-methylxanthine (IBMX) (I5879), insulin from bovine pancreas (I6634), dexamethasone (D1756), Oil Red O (O0625) and haematoxylin (51275). The Annexin V–FITC/PI apoptosis detection kit (40302ES60) and MitoTracker Deep Red FM (40743ES50) were from Yeasen.

Antibodies

Primary antibodies were purchased as follows: p-S6 ribosomal protein (Ser240/244) (D68F8) XP rabbit mAb (5364), ATGL antibody (2138), p-Akt (Ser473) (D9E) XP rabbit mAb (4060), Akt (pan) (C67E7) rabbit mAb (4691), HSL antibody (4107), p-AMPKα (Thr172) (40H9) rabbit mAb (2535), p-HSL (Ser565) antibody (4137), p-HSL (Ser660) antibody (45804), AMPKα antibody (2532), p70 S6K antibody (9202), LAMP1 (D2D11) XP rabbit mAb (9091), p-p70 S6K (Thr389) antibody (9205) and ACSL1 antibody (4047) from Cell Signaling Technology; Abhd5/CGI-58 antibody (ab183739), adipose triglyceride lipase (p-S406) (ab135093), LSDP5 antibody (ab222811), CPT1A antibody (ab128568), APG5L/ATG5 antibody (ab108327), ATG16L1 antibody (ab187671), ATG4B antibody (ab154843) and LC3B antibody (ab192890) from Abcam; PEDFR/PNPLA2/ATGL antibody (NBP2-59390) and ABDH5 antibody (H00051099-M01) from Novus; PLIN3 antibody (GP30) from Progen; P62/SQSTM1 polyclonal antibody (18420-1-AP) from Proteintech; β-actin (M1210-2) and GAPDH (EM1101) from HuaAn Biotechnology; PLIN3 antibody (D194875) from BBI Life Sciences; HILPDA antibody (LS-C144423) from LSBio; zDHHC11 antibody (OAGA02799) from Aviva Systems Biology; ELMOD2 antibody (A7859) from ABclonal; and anti-Flag M2 mAb (F1804) from Millipore Sigma. Secondary antibodies were purchased as follows: streptavidin–horseradish peroxidase (HRP) conjugate (A0303) from Beyotime; anti-HA-tag mAb-HRP-DirecT (M180-7), anti-DDDDK-tag mAb-HRP-DirecT (M185-7), anti-IgG (H + L chain) (rabbit) (458) and anti-IgG (H + L chain) (mouse) (330) from MBL; anti-rabbit IgG (Fc), alkaline phosphatase (AP) conjugate (S3731) and anti-mouse IgG (H + L), AP conjugate (S3721), from Promega; zDHHC11 antibody (PA5-69643), G0S2 antibody (PA5-109748), goat anti-mouse IgG (H + L) highly cross-adsorbed secondary antibody (Alexa Fluor Plus 488) (A32723), goat anti-rabbit IgG (H + L) highly cross-adsorbed secondary antibody (Alexa Fluor Plus 488) (A32731), goat anti-mouse IgG (H + L) cross-adsorbed ReadyProbes secondary antibody (Alexa Fluor 594) (R37121), goat anti-rabbit IgG (H + L) cross-adsorbed ReadyProbes secondary antibody (Alexa Fluor 594) (R37117) and goat anti-guinea pig IgG (H + L) highly cross-adsorbed secondary antibody (Alexa Fluor 594) (A-11076) from Thermo Fisher. Also see Supplementary Table 1.

Cell culture and procedures

HEK293 (from W. Liu's laboratory), HEK293^ATG5-KO (from W. Liu's laboratory), HEK293T (from Q. Sun's laboratory), HepG2 (from W. Liu's laboratory), MEF (from W. Liu's laboratory), MEF^ATG5-KO (from W. Liu's laboratory)[55], 3T3-L1 (from Z. Meng's laboratory), Huh7 (from Q. Sun's laboratory), AML12 (from X. Xu's laboratory), HepG2^zDHHC11-KO (from D. Neculai's laboratory) and HepG2^ATGL.C15S (from D. Neculai's laboratory) cells were cultured in DMEM (Shanghai BasalMedia Technology, L110KJ) supplemented with 10% FBS (Gibco, 10270-106). The cells were maintained at 37 °C in a 5% CO_2 incubator. For starvation procedures, HBSS (Shanghai BasalMedia Technology, B410KJ) was used. For imaging experiments, cells were seeded on 18-mm round glass coverslips (Fisherbrand, 12541005) placed in 12-well plates. HEK293T and HepG2 cells, intended for the ABE assay, underwent transient transfection using PEI (Polysciences, 23966-2) in adherence to the manufacturer's guidelines. Meanwhile, transfections of HepG2, HepG2^zDHHC11-KO, HepG2^ATGL.C15S, Huh7, AML12, HEK293, HEK293^ATG5-KO, MEF and MEF^ATG5-KO cells for imaging purposes were executed with Lipofectamine 3000 (Invitrogen, L3000-015) following the provided protocols.

3T3-L1 cell differentiation

3T3-L1 cells were differentiated as previously described[56]. Briefly, cells were seeded in a six-well plate at a density of 3×10^3 cells per cm^2 and grown in DMEM containing 10% FBS until 70% confluence. To initiate differentiation, we added MDI induction medium (DMEM containing 10% FBS, 0.5 mM IBMX, 0.25 μM dexamethasone and 5 μg ml⁻¹ insulin) on day 0. On day 3, MDI induction medium was replaced with 3 ml of

adipocyte maintenance medium (DMEM containing 10% FBS and 5 µg ml⁻¹ insulin). On day 6, adipocyte maintenance medium was replaced with fresh DMEM containing 10% FBS. Fully differentiated adipocyte-like cells were obtained by days 7–10.

Cloning and plasmid construction

All PCR reactions were performed using Vazyme Biotech 2× Phanta HS Master Mix (VP512-01) and ClonExpress MultiS One Step Cloning Kit (C113-02) according to the manufacturer's instructions. Human ATGL (aa 1–504) cDNA was subcloned into the pEGFP-C1 expression vector (Clontech). Human zDHHC1 (aa 1–485), zDHHC2 (aa 1–367), zDHHC3 (aa 1–299), zDHHC4 (aa 1–344), zDHHC5 (aa 1–715), zDHHC6 (aa 1–413), zDHHC7 (aa 1–308), zDHHC8 (aa 1–765), zDHHC9 (aa 1–364), zDHHC11 (aa 1–412), zDHHC12 (aa 1–267), zDHHC13 (aa 1–622), zDHHC14 (aa 1–488), zDHHC15 (aa 1–337), zDHHC16 (aa 1–377), zDHHC17 (aa 1–632), zDHHC18 (aa 1–388), zDHHC19 (aa 1–309), zDHHC20 (aa 1–365), zDHHC21 (aa 1–265), zDHHC22 (aa 1–263), zDHHC23 (aa 1–409) and zDHHC24 (aa 1–284) cDNAs were subcloned in pEGFP-C1 vector (Clontech) and sequence verified. zDHHC11 (aa 1–412), ATGL (aa 1–504), ATGL^{C15S} (aa 1–504), ATGL$^{C15/61S}$ (aa 1–504), ATGL^{C28S} (aa 1–504), ATGL^{S47A} (aa 1–504), ATGL^{C144S} (aa 1–504), ATGL$^{C144/152S}$ (aa 1–504), ATGL$^{F146A/V150A}$ (aa 1–504), ATGL^{F147A} (aa 1–504), ATGL^{F150A} (aa 1–504), ATGL^{C152S} (aa 1–504), ATGL^{C194S} (aa 1–504), ATGL^{C238S} (aa 1–504), ATGL^{C312S} (aa 1–504), ATGL$^{C312/412S}$ (aa 1–504), ATGL$^{C312/374/412S}$ (aa 1–504), ATGL^{C374S} (aa 1–504), ATGL^{C412S} (aa 1–504), ATGL^{C439S} (aa 1–504), ATGL^{C449S} (aa 1–504) and CGI-58 (aa 1–349) were subcloned in pmCherry-C1 (Clontech). N-terminal HA (3×HA)-epitope-tagged zDHHC11, zDHHC16 and ATGL were introduced by PCR-driven overlap extension, which replaced the GFP from pEGFP-C1 vectors. C-terminal Flag-tagged ATGL was introduced into the pEnter vector by PCR-driven overlap extension. C-terminal Flag-tagged ATGL^{C15S}, ATGL^{C61S}, ATGL$^{C15/61S}$, ATGL^{F147S}, ATGL^{V150A}, ATGL$^{F147S/V150A}$, ATGL^{C144S}, ATGL^{C152S}, ATGL$^{C144/152S}$, ATGL^{C238S}, ATGL^{C312S}, ATGL^{C374S}, ATGL^{C412S}, ATGL$^{C312/412S}$ and ATGL$^{C312/374/412S}$ mutations were introduced by PCR-driven overlap extension, which replaced the ATGL from the pEnter-ATGL-Flag construct. The GFP-LiveDrop plasmid was constructed by inserting a DNA fragment produced by PCR. This fragment, synthesized using overlapping primers, is based on the LD-targeting GPAT4 fragment (5′-CTCACGGTCCTGTGGGGGTTAGGAGTGCTGATTCGG TACTGCTTTCTGCTGCCGCTCAGGATAGCACTGGCTTTCACAGGGATT AGCCTTCTGGTGGTGGGCACAACTGTGGTGGGATACTTGCCAAATGG GAGGTTTAAGGAGTTCATGAGTAAACATGTTCACTTAATGTAA-3′)[1]. It was then subcloned into the pEGFP-C1 vector (Clontech) and subsequently sequence verified. Additionally, an N-terminal Flag-tagged version of LiveDrop was created by replacing the GFP tag with the Flag tag in the pEGFP-C1 vector. The GFP/BFP reporter vector GV248 expressing shRNA targeting human zDHHC11 (shRNA-1: 5′-ACTCCAAT GTCAGACTCATGAA-3′, shRNA-2: 5′-ATTTGCACGTATGGATCTTTC-3′, shRNA-3: 5′-TAATGAGATACTCAAAGGTGGT-3′, shzDHHC11::GFP) and the nonsilencing GV248 control vector (5′-TTCTCCGAACGTGTCACGT-3′, shCtrl::GFP) were purchased from Genechem.

Construction of zDHHC11+(B) gene KO in the HepG2 cell line (HepG2$^{zDHHC11+(B)-KO}$)

The HepG2$^{zDHHC11+(B)-KO}$ cell line was established using the CRISPR/Cas9 system. Specific single guide RNA (sgRNA) sequences (5′-GATCGCGTCCTGCATCGACC-3′) targeting both zDHHC11 open reading frames were designed based on exon sequences proximal to the start codons, using the CRISPR design tool available at https://zlab.bio/guide-design-resources. These sgRNA sequences were then annealed and cloned into the BbsI-digested pX330-puro vector. The resulting pX330-sgRNA construct was sequence verified and subsequently transfected into HepG2 cells. At 72 h after transfection, the cells underwent puromycin selection (1 µg ml⁻¹) for 48 h. Fluorescence-activated cell sorting was then performed using the Beckman MoFlo Astrios

EQ system, with single cells being sorted into individual wells of 96-well plates. These single-cell clones were expanded, and clones deficient in zDHHC11+(B) were identified by Sanger sequencing of the PCR products.

Construction of ATGL^{C15S} knockin in the HepG2 cell line (HepG2^{ATGL,C15S})

The ATGL^{C15S} genomic mutation was introduced into HepG2 cells using the CRISPR/Cas9 and piggyBac-mediated genome editing systems. sgRNAs targeting an area near the C15S mutation site were designed using the CRISPR design tool available at https://zlab.bio/guide-design-resources. Their sequence is 5′-TGTTTCCCCGCGAGAAGACG-3′. The annealed sgRNAs were subsequently cloned into the pX330-U6-Chimeric_BB-CBh-hSpCas9-puro vector following digestion with the BbsI restriction enzyme. For donor construction, two genomic fragments of approximately 500 bp each, upstream and downstream of the TTAA sequence in ATGL's second intron, were amplified. These fragments were inserted into the left and right inverted terminal repeats of the piggyBac transposon. This piggyBac system incorporated a GFP-puro fusion gene for both positive and negative selection. Cells were cotransfected with the sgRNA-Cas9 plasmid and the donor plasmid to facilitate the introduction of the C15S mutation. At 72 h following transfection, cells were trypsinized to create a single-cell suspension, and GFP-positive cells were sorted into 96-well plates using the Beckman MoFlo Astrios EQ flow cytometer. The genomic DNA of these GFP-positive cells was extracted and PCR amplified for regions surrounding the mutation sites. Sequencing of these PCR products identified mutation-corrected clones. To excise the piggyBac cassettes from these corrected clones, we initiated transient transposase expression. Following another round of trypsinization to create single-cell suspensions, GFP-negative cells were sorted into 96-well plates using the same flow cytometer. Seamless removal of the piggyBac transposon, resulting in the restoration of the original second intron without any foreign sequence, was confirmed by DNA sequencing.

Immunofluorescence and microscopy

HepG2, HepG2$^{zDHHC11+(B)-KO}$ and HepG2^{ATGL,C15S} cells were grown on glass coverslips (Fisher, 12-545-100) and fixed using 3% PFA for 20 min at room temperature. For LD visualization, the fixed cells were rinsed three times with PBS and stained with either LipidTOX Red/Deep Red (1:1,000) or BODIPY 493/503 (1:1,000) for 15–30 min at room temperature. After staining, cells were again rinsed three times with PBS. In drug treatments, HepG2, HepG2$^{zDHHC11+(B)-KO}$ and HepG2^{ATGL,C15S} cells on glass coverslips were treated with HBSS starvation medium containing a DGAT1i (T863, 20 µM) or FSK (10 µM) for 24 h and then fixed and stained as above.

For endogenous PLIN3 and ATGL staining, fixed cells were rinsed three times with PBS, permeabilized and blocked with a mixture of 0.1% saponin (BBI Life Sciences, EA21BA005), 10% goat serum (Solarbio, SL050) and 1% BSA (BBI Life Sciences, A600332-0100) in PBS for 1 h at room temperature. This was followed by incubation with primary antibodies—PLIN3 (Progen, GP30, 1:100) or ATGL (Novus, AT18E6, 1:100)—overnight at 4 °C in a solution containing 0.05% saponin, 5% goat serum and 0.5% BSA. After this, cells were rinsed three times with 0.05% saponin in PBS and incubated with secondary antibodies (Thermo Fisher, R37121 or A-11076; 1:500) for 1 h at room temperature. Following incubation, cells were rinsed three times with PBS and stained with BODIPY 493/503 (1:1,000) for 15–30 min, followed by three more rinses with PBS.

To visualize fluorescent-tagged proteins of interest, such as GFP-LiveDrop, GFP-ATGL and GFP-zDHHC, cells were first grown in a 12-well dish containing coverslips. This was followed by transient transfection with the respective plasmids using Lipofectamine 3000 according to the manufacturer's protocol. Approximately 24 h after

transfection, cells were rinsed two times with warm HBSS before being fixed with 4% PFA for 15 min at room temperature. After fixation, excess PFA was removed by rinsing the cells with PBS.

All coverslips were then carefully mounted onto glass slides using 35 μl Fluoromount-G (SouthernBiotech, 0100-01). Imaging was performed using a Zeiss LSM 880 confocal microscope in Airyscan mode, and the acquired images were processed using ZEN Blue software (Zeiss). For the quantification of LDs and subsequent analyses, images were processed following a previously described[57] method using Fiji software[58]. To assess the localization of PLIN3 and ATGL on LDs, we used PixInsight software (https://pixinsight.com) for signal analysis around the periphery of the LDs. Initially, red (PLIN3 or ATGL) and green (BODIPY) channels were separated through channel extraction. In the green channel, LDs were identified using the range selection tool, followed by binarization and expansion by 3 pixels to create a mask. This mask was then applied to both the red channel and the original green channel. Pixel intensities outside the mask were set to zero using curve transformation. The total signal intensity within the mask was then measured and recorded.

LD staining and quantification

For Red C12 pulse–chase experiments, a protocol was used as previously described[28]. Briefly, cells were cultured in 12-well plates and treated with 2 μM BODIPY 558/568 C12 (Molecular Probes) in regular medium containing 10% serum (CM) for 16 h. After this, the cells were washed three times with CM. They were then incubated in either CM or starvation medium (HBSS) for 24–48 h. Following this incubation, 100 nM of either MitoTracker or LysoTracker was added for 30 min, after which cells were washed three times with PBS and fixed using 3% PFA (Electron Microscopy Sciences, 15710). For LD staining, either Lipid-TOX Red/Deep Red (1:1,000) or BODIPY 493/503 (1:1,000) was added directly to the PFA-fixed cells and allowed to incubate for 15–30 min. To quantify the LDs, we imaged the cells that were either stained with BODIPY 558/568 C12 or fixed and then labelled with LipidTOX Red/Deep Red or BODIPY 493/503, using a Zeiss LSM 880 confocal microscope. Image analysis was conducted using Fiji software[58].

Isolation of LDs positive for LiveDrop

HepG2, HepG2^zDHHC11-KO and HepG2^ATGL.C15S cells were cultured in 10-cm dishes, and LDs were isolated as described by Ding et al.[59], with minor modifications. Cells were transfected with plasmids encoding Flag-LiveDrop using the PEI transfection reagent. After 48 h, cells expressing the Flag-tagged LiveDrop protein were collected and washed with ice-cold PBS. Cell pellets were resuspended in lysis buffer containing 20 mM tricine, 250 mM sucrose and 1 mM EDTA and supplemented with 1 mM freshly prepared phenylmethylsulfonyl fluoride (PMSF), protease inhibitor cocktail (Bimake, B14001), and phosphatase inhibitors A and B (Bimake, B15001-A, B15001-B). The suspension was incubated on ice for 20 min, followed by mechanical disruption using a glass Dounce homogenizer with 80–100 strokes. The homogenate was then centrifuged at 3,000g for 10 min at 4 °C to obtain the postnuclear supernatant fraction. A 10-ml volume of the postnuclear supernatant fraction was carefully layered over 2 ml of cushion buffer (20 mM HEPES, 100 mM KCl, 2 mM MgCl$_2$, pH 7.4) in an SW41 Ti ultra-centrifuge tube (Beckman, 344060). The samples were subjected to ultracentrifugation at 182,000g for 1 h at 4 °C. The supernatants were collected and incubated with anti-Flag affinity beads (Bimake, B23102) for 3 h at 4 °C with gentle agitation. After incubation, the beads were washed five times with lysis buffer supplemented with protease inhibitors (Bimake, B14001). Finally, the immunoprecipitated samples were eluted and analysed by western blotting (WB).

Western blotting

For sample preparation of whole-cell lysates, HepG2 cells from one well of a six-well plate (WT, HepG2^zDHHC11+(B)-KO and HepG2^ATGL.C15S) were rinsed with PBS and lysed in 200 μl RIPA buffer (50 mM Tris, 150 mM NaCl, 1% NP-40, 0.5% sodium deoxycholate, 0.1% SDS, 1 mM EDTA) supplemented with freshly prepared 1 mM PMSF, protease inhibitors (Bimake, B14001), and phosphatase inhibitors A and B (Bimake, B15001-A, B15001-B) for 1 h. For the preparation of liver lysate samples, livers were excised from mice and then cut into small pieces. These pieces were washed three times with HBSS. A 1 mg ml⁻¹ collagenase solution (Sigma, C0130) in HBSS was prepared, and the liver pieces were digested at 37 °C for 4–18 h to ensure complete digestion. Subsequently, the samples were centrifuged at 1,600g at 4 °C for 5 min. The resultant liver cell pellets were again washed three times with HBSS, followed by lysis using a buffer comprising 50 mM Tris–HCl (pH 7.4), 1% Triton X-100, 0.2% sodium deoxycholate, 0.2% SDS and 1 mM EDTA. This lysis buffer was supplemented with 1 mM freshly prepared PMSF, protease inhibitors (Bimake, B14001), and phosphatase inhibitors A and B (Bimake, B15001-A, B15001-B) for 1 h. The lysates were then centrifuged at 10,000g at 4 °C for 10 min. The supernatants were collected, and protein content was determined using the BCA protein quantification kit (Yeasen, 2020IES86). Subsequently, 5× sample buffer containing β-mercaptoethanol was added, and samples were boiled for 5–7 min. Proteins (40 μg) from each sample were loaded onto either 8% or 10% gels and separated by SDS–PAGE at 100 V for 2 h. Proteins were transferred onto polyvinylidene difluoride membranes at 120 V for 1 h. The membranes were blocked using 1% BSA and incubated overnight at 4 °C with the primary antibodies, all at a dilution of 1:1,000 in 1% BSA–TBST. Following primary antibody incubation, membranes were washed four times with 0.1% BSA–TBST. They were then incubated with secondary antibodies (diluted 1:5,000)—mouse HRP (MBL, 330), rabbit HRP (MBL, 458), mouse AP (Promega, S3721) or rabbit AP (Promega, S3731)—in 1% BSA. Following incubation, four additional washes were performed using 0.1% TBST. For protein detection, membranes incubated with HRP were treated with SuperSignal West Pico PLUS (Thermo Fisher, 43580). Those incubated with AP were treated with AP staining buffer (100 mM Tris–HCl, 5 mM MgCl$_2$, 50 mM NaCl, 20 mg ml⁻¹ BCIP, 40 mg ml⁻¹ NBT at pH 9.5).

TAG detection

Cells were cultured in 10-cm dishes until they reached 90% confluence. They were then collected by scraping and washed once with PBS. Cellular lipids were extracted by lysing the cells in a lipid extraction solution composed of a hexane and isopropanol mixture (volume ratio 3:2). The lysate was centrifuged at 1,000g for 5 min. For lipid extraction from tissues, 30-mg tissue fragments were added to 1.5 ml of an extraction solution (isopropanol, double-distilled water (ddH$_2$O) and Triton X-100 at a volume ratio of 5:2:2). The tissues were then minced using a tissue grinder (Tocan, LC000948). After grinding, the mixture was centrifuged at 19,400g for 5 min. The upper organic phase was carefully transferred to new Eppendorf tubes. The collected lipids were dried using a pressure blowing concentrator with N$_2$ gas. Once dried, the lipids were resuspended in CHCl$_3$ containing 1% Triton X-100 and then dried again using the pressure blowing concentrator. For the final step, the lipids were resuspended in ddH$_2$O containing 1% Triton X-100. The extracted lipids were then analysed using the EnzyChrom triglyceride assay kit (Bioassay Systems, ETGA-200) to detect TAG contents.

Glycerol release assay

Glycerol release was measured in HepG2 (WT, HepG2^zDHHC11+(B)-KO and HepG2^ATGL.C15S) cells using a lipolysis assay kit (Abcam, ab185433) according to the manufacturer's protocol.

RT–qPCR analysis assay

From mice infected with AAV, liver tissues were procured to extract total RNAs. The extraction was done using the GeneJET RNA purification kit (Thermo Fisher, K0732). Separately, HepG2 cells underwent transfection with three distinct ATGL shRNAs (shRNA-1: 5′-CCCT

TTACTCCTGAGAACTTT-3′, shRNA-2: 5′-GCACCTGTGCCTTAATC TTCC-3′, shRNA-3: 5′-GGACCAAGATTCTTGGTAAAT-3′) through PEI, in adherence to the manufacturer's guidelines. Total RNAs from 16 collected HCC clinical liver tissues were also extracted in the same manner. Subsequently, cDNAs were synthesized using the SuperScript VILO cDNA kit (Thermo Fisher, 11754250) following the manufacturer's instructions. These cDNAs were used for RT–qPCR using the Taqman Fast Advanced Master Mix (Applied Biosystems, 4444557) and a predesigned Taqman probe specific to hATGL (human *ATGL* gene), hzDHHC11 (human *ZDHHC11* gene), mATGL (mouse *Atgl* gene) and mzDHHC11 (mouse *Zdhhc11* gene), with normalization to hGAPDH or mGAPDH. hATGL expression was detected with the forward primer qPCR-hATGL-Fw (GACAGCTC CACCAACATCCA) and the reverse primer qPCR-hATGL-Rv (GAGGCG GTAGAGGTTGCGCA); hzDHHC11 expression was detected with the forward primer qPCR-hzDHHC11-Fw (CGCCCTGGGCTCATCTGCAC) and the reverse primer qPCR-hzDHHC11-Rv (TCATCCCCTTCCCGT GCCGT); endogenous mATGL expression was detected with the forward primer qPCR-mATGL-Fw (TGCACCAATGTGGCCTTCCC) and the reverse primer qPCR-mATGL-endo-Rv (GGGGCAGACAGGATCTT GTT); exogenous mATGL expression was detected with the forward primer qPCR-mATGL-Fw (TGCACCAATGTGGCCTTCCC) and the reverse primer qPCR-mATGL-oe-Rv (CTTCCAGGGTCAAGGAAGGC); exogenous mzDHHC11 expression was detected with the forward primer qPCR-mzDHHC11-Fw (CATCCAGCAGAGGAGAAAGAGC) and the reverse primer qPCR-mzDHHC11-Rv (TCGGCGAAAGAGTAGACACTGG). The qPCR procedure was executed in the StepOne real-time PCR system (Applied Biosystems), spanning 40 cycles at 95 °C for 1 s and 60 °C for 20 s. The relative mRNA quantities were calculated using the comparative $2^{-\Delta\Delta Ct}$ method.

IP and WB analysis

HEK293T cells were cotransfected with either zDHHC11 and ATGL or zDHHC16 and ATGL plasmids. At 48 h after transfection, cells were collected, rinsed with cold PBS and lysed using lysis buffer containing 50 mM Tris–HCl (pH 7.5), 150 mM NaCl, 1 mM $MgCl_2$, 1% NP-40, protease inhibitors (Bimake, B14001), and phosphatase inhibitors A and B (Bimake, B15001-A, B15001-B). Afterwards, the supernatants were isolated and incubated with anti-Flag beads (Bimake, B23102) at 4 °C for 3 h. These beads were then thoroughly washed seven times with a washing buffer composed of 50 mM Tris–HCl (pH 7.5), 150 mM NaCl, 1 mM $MgCl_2$ and protease inhibitors (Bimake, B14001) maintained at 4 °C. The immunoprecipitated samples were then subjected to WB analysis using anti-DDDDK-tag mAb-HRP-DirecT (MBL, M185-7; dilution 1:5,000) and anti-HA-tag mAb-HRP-DirecT (MBL, M180-7; dilution 1:5,000) antibodies.

ABE assay

The ABE assay was conducted as previously described[60], with slight modifications. HEK293T cells transiently expressing 3×HA-tagged ATGL or differentiated 3T3-L1 cells were treated with 2-BP (50 µM) or dimethylsulfoxide (DMSO) as a negative control for 18 h and collected 48 h after transfection. HepG2 cells, both WT and zDHHC11-KO (HepG2$^{zDHHC11\text{-}KO}$), were transiently transfected with Flag-tagged ATGL plasmids and collected after 48 h. Moreover, HEK293T cells transiently expressing various Flag-tagged ATGL mutants were collected 48 h after transfection. HepG2 and HepG2$^{ATGL.C15S}$ cells were collected once they reached a confluence between 90% and 100%. Before lysis, NEM was dissolved in 100% ethanol and added to the lysis buffer containing 50 mM Tris–HCl (pH 7.5), 150 mM NaCl, 1 mM $MgCl_2$, 1% NP-40, 10% glycerol, protease inhibitors (Bimake, B14001), and phosphatase inhibitors A and B (Bimake, B15001-A, B15001-B) to achieve a final concentration of 50 mM. Cells were subsequently suspended in this NEM-supplemented lysis buffer for 1.5 h at 4 °C. The supernatants were incubated with anti-Flag beads (Bimake, B23102) or ATGL antibody-coated beads at

4 °C for 3 h. Following this, the beads underwent multiple washing stages (five times with lysis buffer pH 7.5, three times with lysis buffer pH 7.2), followed by incubation in freshly prepared HAM-containing lysis buffer (50 mM Tris–HCl, pH 7.2, 150 mM NaCl, 1 mM $MgCl_2$, 1% NP-40, 10% glycerol, 1 mM HAM and protease inhibitor) at room temperature for 1 h. This was succeeded by four washes with lysis buffer pH 7.2 and three washes with lysis buffer pH 6.2. Thereafter, beads were treated with biotin-BMCC (5 µM) in lysis buffer (pH 6.2) at 4 °C for 1 h. WB analysis of the immunoprecipitated samples was performed using anti-Flag M2 antibody (Millipore Sigma, F1804; dilution 1:4,000), ATGL antibody (Cell Signaling Technology, 2138) and streptavidin–HRP (A0303, Beyotime; dilution 1:5,000).

OCR detection

Seahorse XFp Cell Mito Stress Tests (Agilent Technologies) were conducted according to the manufacturer's instructions. HepG2 cells (WT, HepG2$^{zDHHC11+(B)\text{-}KO}$ and HepG2$^{ATGL.C15S}$) were seeded in a Seahorse XF96 plate (Seahorse Bioscience) at a density of 10,000 cells per well 24 h before the assay. Subsequently, the XF96 medium was augmented with 2 µM rotenone, 1 µM fluoro-carbonyl cyanide phenylhydrazone (FCCP) and 1 µg ml⁻¹ oligomycin. The compounds were introduced into the medium at predetermined time points. The OCR was subsequently assessed using the Seahorse Bioscience XF96 extracellular flux analyser. Basal respiration was determined before the addition of oligomycin, and proton leak was evaluated following oligomycin treatment. ATP production was calculated by determining the difference between the basal respiration and proton leak. Following the FCCP treatment, the spare respiratory capacity was ascertained by calculating the difference between the maximal respiration and ATP production.

Expression of WT and mutant ATGL in HEK293T cells

HEK293T cells, cultivated in six-well plates, were grown in DMEM supplemented with 5% FBS. The cells were transiently transfected with plasmid DNA encoding either WT ATGL or its variants, using JetOptimus (Sartorius) as the transfection agent. To enhance the accumulation of palmitoylated ATGL protein variants, we treated the cells with 100 µM palmostatin B (Sigma) for 4 h before cell lysis. For lysis, cells were subjected to ultrasonication in an ice-cold lysis buffer containing 250 mM sucrose, 1 mM EDTA (pH 7.0), 1 mM dithiothreitol (DTT), EDTA-free protease inhibitor cocktail (Roche) and 1 mM PMSF. After lysis, cell lysates were centrifuged at 12,000g for 10 min. The supernatant containing the solubilized proteins was then analysed for ATGL expression. The presence of ATGL variants was detected by WB using an anti-GFP antibody (Proteintech) in accordance with the manufacturer's protocol.

TAG hydrolase activity assays

Glyceryl trioleate (triolein) (cat. no. T7140) was obtained from Sigma. [9,10(N)-³H]Glycerol trioleate (cat. no. NET431001MC SBF3, lot no. 3125402) along with egg phosphatidylcholine (#840051) and brain phosphatidylserine (#840032) were obtained from Avanti Polar Lipids.

Briefly, HEK293T cells, grown attached in six-well plates in DMEM with 5% FBS, were transiently transfected with a cocktail containing plasmid DNA and JetOptimus (Sartorius) as the transfection agent. The cells were treated with 100 µM palmostatin B (Sigma) for 4 h to enrich the samples with S-acylated ATGL before lysis. Cells were lysed in an ultrasonic ice bath in a buffer containing 250 mM sucrose, 1 mM EDTA (pH 7.0), 1 mM DTT, EDTA-free protease inhibitor (Roche) and 1 mM PMSF. The lysates were centrifuged at 12,000g for 10 min, and the protein concentration was determined by the BCA assay using the Pierce BCA protein assay kit. The expression of ATGL and its mutants in the solubilized fraction was assessed by WB using an anti-GFP antibody (Proteintech) following the manufacturer's instructions.

TAG hydrolase activity assays were performed essentially as described by Schweiger et al.[38], with minor modifications. The TAG substrate consisted of 1 mM triolein containing 11.25 µCi ml⁻¹ [9,10(N)-³H]

glycerol trioleate as a tracer and 109 µM of a 3:1 phosphatidylcholine/phosphatidylserine mixture in 0.1 M potassium phosphate buffer (pH 7.0). Emulsions were prepared on ice by first sonicating the sample for 30 s to disperse the lipids in the phosphate buffer and then agitated using a benchtop vortex for 30 s. The emulsion-containing solution was allowed to sit for 30 min before being aliquoted into 1.5-ml microcentrifuge tubes. Each aliquot was supplemented with fatty acid-free BSA (Sigma-Aldrich) to reach a final concentration of 5% (w/v). To determine the TAG hydrolase activity, we incubated 50 µg of the total protein lysate in a total volume of 25 µl sucrose solution (250 mM sucrose, 1 mM EDTA, pH 7.0, 1 mM DTT) for 60 min at 37 °C after adding the same volume of emulsified 1 mM triolein substrate to obtain 50 µl of the final reaction mixture. As a negative control, 25 µl sucrose solution was mixed with 25 µl substrate solution (50 µl reaction mixture). The enzymatic reactions were terminated by adding 650 µl of CH_3OH/$CHCl_3$/n-heptane (10:9:7) and 200 µl of 0.1 M K_2CO_3 (pH 10.5). Fatty acid extraction was performed by mixing the samples vigorously for 5 s, followed by centrifugation at 500g at room temperature for 10 min. An aliquot of 200 µl of the upper aqueous phase was transferred into scintillation vials containing 4 ml EcoLite scintillation cocktail (MP Biomedicals). Radioactivity was determined by liquid scintillation counting using a Tri-Carb 2910 TR liquid scintillation analyser (PerkinElmer). Counts generated from blank measurements were subtracted, and the rates of TAG hydrolase activity, presented as micromoles of released fatty acids per hour per milligram of protein, were calculated according to Schweiger et al.[38].

ATGL activity assay using EnzChek substrate

HepG2 cells were cultured to 80% confluence in a 10-cm dish in EMEM supplemented with 10% FBS. Cells were transiently transfected with a plasmid expressing pEGFP-C1, GFP-ATGL or GFP-ATGL^{C15S} using the Viafect transfection reagent according to the manufacturer's protocol. At 16 h after transfection, cells were collected into cold PBS and lysed in 20 mM Tris−HCl and 0.0125% Zwittergent 3-18 by serial passage through a 30-gauge syringe. Protein concentration was normalized to 2.0 mg ml^{-1}. The concentration of recombinant protein lysate was determined using a BCA assay. The SpectraMax M5e plate reader and SoftMax Pro 5.4.1 software from Molecular Devices were used for fluorescence measurements. To calibrate the instrument for the ATGL activity assay, we performed both the excitation and emission sweeps on the fluorescent standard 4,4-difluoro-5-methyl-4-bora-3a,4a-diaza-s-indacene-3-dodecanoic acid (BODIPY 500/510 C1, C12, abbreviation BODIPY-C12). The maximum excitation/emission wavelengths were 482 nm/515 nm with a 495-nm filter cutoff. The ATGL activity assay was adapted from the lipoprotein lipase assay of Basu et al.[61]. Briefly, the assay was carried out at 37 °C in a black 96-well plate. Recombinant protein lysate (50 µg) was incubated with 0.62 µM EnzChek lipase substrate in the presence of 0.15 M NaCl, 20 mM Tris−HCl, pH 8.0, 0.0125% Zwittergent and 1.5% fatty acid-free BSA in a total volume of 100 µl. A 4× working solution was freshly prepared with 0.6 M NaCl, 80 mM Tris−HCl, pH 8.0, and 6% fatty acid-free BSA. The EnzChek lipase substrate was stored in DMSO at −20 °C. The EnzChek lipase substrate solution was freshly prepared in 0.05% Zwittergent for each use. Reactions were carried out in triplicate, and experiments were repeated three times.

Mouse AAV infection and feeding protocols

All animal experiments were approved by the Institutional Animal Care and Use Committee at the Zhejiang University School of Medicine (AIRB-2021-1037). C57BL/6J mice (6–8 weeks old) of both sexes were used. Mice were group housed (two to five per cage) under standard conditions (40% humidity, 22 ± 2 °C, 12-h reversed light/dark cycle, chow diet (Xietong Shengwu, SZS9126-1010082) and water ad libitum). To investigate the effects of zDHHC11 overexpression and ATGL palmitoylation deficiency on liver metabolism under diet-induced obesity, we fed the mice with an HFD (Research Diets, D12492) for 3 months. At

12 weeks after AAV infections, mice were fasted for 6 h, and their livers were collected for protein and RNA extraction or triglyceride quantification. AAVs (AAV9-TBG-GFP control (AAV-control virus), AAV9-TBG-GFP with mzDHHC11 gene overexpression (AAV-mzDHHC11), AAV9-TBG-GFP with both endogenous mATGL knockdown and exogenous mATGL gene overexpression (AAV-shATGL$_{endo}$::mATGL$_{exo}$) and AAV9-TBG-GFP with endogenous mATGL knockdown and exogenous mATGL$_{exo}^{C15S}$ gene overexpression (AAV-shATGL$_{endo}$::mATGL$_{exo}^{C15S}$)) were acquired from Vigene Biosciences. The mATGL shRNA (shATGL$_{endo}$) (GGAGAGAACGTCATCATATTTCAAGAGAATATGATGACGTTCTCTCTTTTTT) was targeted to endogenous mATGL but not to exogenous mATGL because the shATGL$_{endo}$-targeted fragments on the mATGL$_{exo}$ gene had been modified according to codon preference.

C57BL/6J mice (aged 6–8 weeks) were intraperitoneally injected with 4×10^{11} vector genomes (vg) of virus per mouse, diluted in 200 µl PBS. After infection:

- A group of 14 male mice (7 infected with AAV-control virus and 7 with AAV-mzDHHC11) were maintained on a regular diet.
- Another group of 14 female mice (7 infected with AAV-control virus and 7 with AAV-mzDHHC11) were maintained on a regular diet.
- Another group of 14 male mice (7 infected with AAV-control and 7 with AAV-mzDHHC11) were subjected to HFD feeding for 3 months.
- A set of 12 male mice (7 with AAV-shmATGL$_{endo}$::mATGL$_{exo}$ and 5 with AAV-shmATGL$_{endo}$::mATGL$_{exo}^{C15S}$) followed a regular diet.
- Another set of 17 male mice (8 with AAV-shmATGL$_{endo}$::mATGL$_{exo}$ and 9 with AAV-shmATGL$_{endo}$::mATGL$_{exo}^{C15S}$) were given HFD feeding for 3 months.

Oil Red O staining

Mice infected with AAV were killed, and fresh liver tissues were collected for Oil Red O staining. Cryosections of these tissues, ranging from 8 to 18 µm in thickness, were prepared and mounted on slides. These slides were then immersed in absolute propylene glycol for 5 min. Subsequently, they were stained with an Oil Red O solution heated to 60 °C. This staining solution was prepared by dissolving 0.5 g Oil Red O (Sigma, O0625) in 10 ml isopropanol (>98% purity) and then diluting it to a 60% concentration using ddH$_2$O. After the staining process, the slides were differentiated in 85% propylene glycol solution for 1 min, followed by two rinses with ddH$_2$O. For enhanced contrast, the slides were counterstained with haematoxylin (Sigma, 51275) for 1–2 min, rinsed thoroughly with tap water and then rinsed two more times with distilled water. The final step involved mounting the slides using an aqueous mounting medium, after which they were ready for observation and imaging under an Olympus BX61 microscope.

Statistics

For in vivo studies, littermates were randomly assigned to treatment groups. No randomization was performed for in vitro experiments. Sample sizes were based on previous experiments in the field[62] and are indicated in the respective figure legends. No animals or data points were excluded from analyses, and investigators were not blinded to treatment allocation during experiments or outcome assessments. Unless stated otherwise, all biological replicates had a minimum of three samples, denoted as n in the figure legends. For cell culture experiments, RNA and protein analyses were performed with two to three technical replicates. Data are presented as mean ± s.e.m. unless specified differently. Normal distribution of data was assumed but not formally tested. For comparisons between two groups, two-tailed unpaired or paired Student's t tests were applied assuming a normal distribution. One-way analysis of variance (ANOVA) and Tukey's post hoc tests were used for comparisons across multiple groups with normally distributed data. GraphPad Prism 8 software executed all

statistical analyses, reporting exact *P* values for significant differences and 'NS' for nonsignificant results. Densitometric quantification was performed using Fiji software[58]. Unless noted otherwise, immunoblots are representative of three independent experiments.

Reporting summary

Further information on research design is available in the Nature Portfolio Reporting Summary linked to this article.

Data availability

All DNA constructs in this study are available on request. All other data needed to evaluate the conclusions in the paper are presented herein or in the supplementary materials. All other data supporting the findings of this study are available from the corresponding authors on reasonable request. Source data are provided with this paper.

References

1. Walther, T. C., Chung, J. & Farese, R. V. Jr Lipid droplet biogenesis. *Annu. Rev. Cell Dev. Biol.* **33**, 491–510 (2017).
2. Kory, N., Farese, R. V. Jr & Walther, T. C. Targeting fat: mechanisms of protein localization to lipid droplets. *Trends Cell Biol.* **26**, 535–546 (2016).
3. Thiam, A. R., Farese, R. V. Jr & Walther, T. C. The biophysics and cell biology of lipid droplets. *Nat. Rev. Mol. Cell Biol.* **14**, 775–786 (2013).
4. Herms, A. et al. Cell-to-cell heterogeneity in lipid droplets suggests a mechanism to reduce lipotoxicity. *Curr. Biol.* **23**, 1489–1496 (2013).
5. Zechner, R., Madeo, F. & Kratky, D. Cytosolic lipolysis and lipophagy: two sides of the same coin. *Nat. Rev. Mol. Cell Biol.* **18**, 671–684 (2017).
6. Grabner, G. F., Xie, H., Schweiger, M. & Zechner, R. Lipolysis: cellular mechanisms for lipid mobilization from fat stores. *Nat. Metab.* **3**, 1445–1465 (2021).
7. Carr, R. M. & Ahima, R. S. Pathophysiology of lipid droplet proteins in liver diseases. *Exp. Cell Res.* **340**, 187–192 (2016).
8. Krahmer, N., Farese, R. V. Jr & Walther, T. C. Balancing the fat: lipid droplets and human disease. *EMBO Mol. Med.* **5**, 973–983 (2013).
9. Onal, G., Kutlu, O., Gozuacik, D. & Emre, S. D. Lipid droplets in health and disease. *Lipids Health Dis.* **16**, 128 (2017).
10. Smirnova, E. et al. ATGL has a key role in lipid droplet/adiposome degradation in mammalian cells. *EMBO Rep.* **7**, 106–113 (2006).
11. Zimmermann, R. et al. Fat mobilization in adipose tissue is promoted by adipose triglyceride lipase. *Science* **306**, 1383–1386 (2004).
12. Vaughan, M., Berger, J. E. & Steinberg, D. Hormone-sensitive lipase and monoglyceride lipase activities in adipose tissue. *J. Biol. Chem.* **239**, 401–409 (1964).
13. Lass, A. et al. Adipose triglyceride lipase-mediated lipolysis of cellular fat stores is activated by CGI-58 and defective in Chanarin–Dorfman syndrome. *Cell Metab.* **3**, 309–319 (2006).
14. Yang, X. et al. The G_0/G_1 switch gene 2 regulates adipose lipolysis through association with adipose triglyceride lipase. *Cell Metab.* **11**, 194–205 (2010).
15. Ahmadian, M. et al. Desnutrin/ATGL is regulated by AMPK and is required for a brown adipose phenotype. *Cell Metab.* **13**, 739–748 (2011).
16. Pagnon, J. et al. Identification and functional characterization of protein kinase A phosphorylation sites in the major lipolytic protein, adipose triglyceride lipase. *Endocrinology* **153**, 4278–4289 (2012).
17. Spinelli, M., Fusco, S. & Grassi, C. Nutrient-dependent changes of protein palmitoylation: impact on nuclear enzymes and regulation of gene expression. *Int. J. Mol. Sci.* **19**, 3820 (2018).
18. Sanders, S. S. et al. Curation of the mammalian palmitoylome indicates a pivotal role for palmitoylation in diseases and disorders of the nervous system and cancers. *PLoS Comput. Biol.* **11**, e1004405 (2015).
19. Suzuki, M. et al. ELMOD2 is anchored to lipid droplets by palmitoylation and regulates adipocyte triglyceride lipase recruitment. *Mol. Biol. Cell* **26**, 2333–2342 (2015).
20. Martin, S., Driessen, K., Nixon, S. J., Zerial, M. & Parton, R. G. Regulated localization of Rab18 to lipid droplets: effects of lipolytic stimulation and inhibition of lipid droplet catabolism. *J. Biol. Chem.* **280**, 42325–42335 (2005).
21. Blanc, M. et al. SwissPalm: protein palmitoylation database. *F1000Res* **4**, 261 (2015).
22. de Moura E Dias, M. et al. Diet-induced obesity in animal models: points to consider and influence on metabolic markers. *Diabetol. Metab. Syndr.* **13**, 32 (2021).
23. Casimiro, I., Stull, N. D., Tersey, S. A. & Mirmira, R. G. Phenotypic sexual dimorphism in response to dietary fat manipulation in C57BL/6J mice. *J. Diabetes Complications* **35**, 107795 (2021).
24. Zhang, S. et al. The regulation, function, and role of lipophagy, a form of selective autophagy, in metabolic disorders. *Cell Death Dis.* **13**, 132 (2022).
25. Nguyen, T. B. et al. DGAT1-dependent lipid droplet biogenesis protects mitochondrial function during starvation-induced autophagy. *Dev. Cell* **42**, 9–21 (2017).
26. Schott, M. B. et al. Lipid droplet size directs lipolysis and lipophagy catabolism in hepatocytes. *J. Cell Biol.* **218**, 3320–3335 (2019).
27. Singh, R. et al. Autophagy regulates lipid metabolism. *Nature* **458**, 1131–1135 (2009).
28. Rambold, A. S., Cohen, S. & Lippincott-Schwartz, J. Fatty acid trafficking in starved cells: regulation by lipid droplet lipolysis, autophagy, and mitochondrial fusion dynamics. *Dev. Cell* **32**, 678–692 (2015).
29. Schott, M. B. et al. β-Adrenergic induction of lipolysis in hepatocytes is inhibited by ethanol exposure. *J. Biol. Chem.* **292**, 11815–11828 (2017).
30. Watt, M. J. et al. Regulation of HSL serine phosphorylation in skeletal muscle and adipose tissue. *Am. J. Physiol. Endocrinol. Metab.* **290**, E500–E508 (2006).
31. Gaidhu, M. P. Prolonged AICAR-induced AMP-kinase activation promotes energy dissipation in white adipocytes: novel mechanisms integrating HSL and ATGL. *J. Lipid Res.* **50**, 704–715 (2009).
32. Olzmann, J. A., Richter, C. M. & Kopito, R. R. Spatial regulation of UBXD8 and p97/VCP controls ATGL-mediated lipid droplet turnover. *Proc. Natl Acad. Sci. USA* **110**, 1345–1350 (2013).
33. Nagy, H. M. et al. Adipose triglyceride lipase activity is inhibited by long-chain acyl-coenzyme A. *Biochim. Biophys. Acta* **1841**, 588–594 (2014).
34. Niso-Santano, M. et al. Unsaturated fatty acids induce non-canonical autophagy. *EMBO J.* **34**, 1025–1041 (2015).
35. Samovski, D. & Abumrad, N. A. Regulation of lipophagy in NAFLD by cellular metabolism and CD36. *J. Lipid Res.* **60**, 755–757 (2019).
36. Drisdel, R. C., Alexander, J. K., Sayeed, A. & Green, W. N. Assays of protein palmitoylation. *Methods* **40**, 127–134 (2006).
37. Martinez-Lopez, N. et al. Autophagy in the CNS and periphery coordinate lipophagy and lipolysis in the brown adipose tissue and liver. *Cell Metab.* **23**, 113–127 (2016).
38. Schweiger, M. et al. Measurement of lipolysis. *Methods Enzymol.* **538**, 171–193 (2014).
39. Ren, W., Jhala, U. S. & Du, K. Proteomic analysis of protein palmitoylation in adipocytes. *Adipocyte* **2**, 17–28 (2013).

40. Barajas-Olmos, F. et al. Altered DNA methylation in liver and adipose tissues derived from individuals with obesity and type 2 diabetes. *BMC Med. Genet.* **19**, 28 (2018).

41. Najt, C. P. et al. Lipid droplet-derived monounsaturated fatty acids traffic via PLIN5 to allosterically activate SIRT1. *Mol. Cell* **77**, 810–824 (2020).

42. Sathyanarayan, A., Mashek, M. T. & Mashek, D. G. ATGL promotes autophagy/lipophagy via SIRT1 to control hepatic lipid droplet catabolism. *Cell Rep.* **19**, 1–9 (2017).

43. Khan, S. A. et al. ATGL-catalyzed lipolysis regulates SIRT1 to control PGC-1α/PPAR-α signaling. *Diabetes* **64**, 418–426 (2015).

44. Rambold, A. S., Kostelecky, B., Elia, N. & Lippincott-Schwartz, J. Tubular network formation protects mitochondria from autophagosomal degradation during nutrient starvation. *Proc. Natl Acad. Sci. USA* **108**, 10190–10195 (2011).

45. Xie, X. et al. Identification of a novel phosphorylation site in adipose triglyceride lipase as a regulator of lipid droplet localization. *Am. J. Physiol. Endocrinol. Metab.* **306**, E1449–E1459 (2014).

46. George, J., Soares, C., Montersino, A., Beique, J.-C. & Thomas, G. M. Palmitoylation of LIM kinase-1 ensures spine-specific actin polymerization and morphological plasticity. *eLife* **4**, e06327 (2015).

47. Zhang, M. et al. A STAT3 palmitoylation cycle promotes T$_H$17 differentiation and colitis. *Nature* **586**, 434–439 (2020).

48. Rossin, A. et al. Fas palmitoylation by the palmitoyl acyltransferase DHHC7 regulates Fas stability. *Cell Death Differ.* **22**, 643–653 (2015).

49. Runkle, K. B. et al. Inhibition of DHHC20-mediated EGFR palmitoylation creates a dependence on EGFR signaling. *Mol. Cell* **62**, 385–396 (2016).

50. Robinson, J. W. et al. PI4KIIα phosphorylation by GSK3 directs vesicular trafficking to lysosomes. *Biochem. J.* **464**, 145–156 (2014).

51. Barylko, B. et al. Palmitoylation controls the catalytic activity and subcellular distribution of phosphatidylinositol 4-kinase IIα. *J. Biol. Chem.* **284**, 9994–10003 (2009).

52. Navarro-Lérida, I. et al. Palmitoylation of inducible nitric-oxide synthase at Cys-3 is required for proper intracellular traffic and nitric oxide synthesis. *J. Biol. Chem.* **279**, 55682–55689 (2004).

53. Corvi, M. M., Soltys, C. L. & Berthiaume, L. G. Regulation of mitochondrial carbamoyl-phosphate synthetase 1 activity by active site fatty acylation. *J. Biol. Chem.* **276**, 45704–45712 (2001).

54. Wu, J. W. et al. Deficiency of liver adipose triglyceride lipase in mice causes progressive hepatic steatosis. *Hepatology* **54**, 122–132 (2011).

55. Chang, C. et al. AMPK-dependent phosphorylation of GAPDH triggers Sirt1 activation and is necessary for autophagy upon glucose starvation. *Mol. Cell* **60**, 930–940 (2015).

56. Yang, F. et al. Fas signaling in adipocytes promotes low-grade inflammation and lung metastasis of colorectal cancer through interaction with Bmx. *Cancer Lett.* **522**, 93–104 (2021).

57. Xu, D. et al. Rab18 promotes lipid droplet (LD) growth by tethering the ER to LDs through SNARE and NRZ interactions. *J. Cell Biol.* **217**, 975–995 (2018).

58. Schindelin, J. et al. Fiji: an open-source platform for biological-image analysis. *Nat. Methods* **9**, 676–682 (2012).

59. Ding, Y. et al. Isolating lipid droplets from multiple species. *Nat. Protoc.* **8**, 43–51 (2013).

60. Lu, Y. et al. Palmitoylation of NOD1 and NOD2 is required for bacterial sensing. *Science* **366**, 460–467 (2019).

61. Basu, D., Manjur, J. & Jin, W. Determination of lipoprotein lipase activity using a novel fluorescent lipase assay. *J. Lipid Res.* **52**, 826–832 (2011).

62. Ding, L. et al. Peroxisomal β-oxidation acts as a sensor for intracellular fatty acids and regulates lipolysis. *Nat. Metab.* **3**, 1648–1661 (2021).

Author contributions

D.N., G.D.F. and B.R. designed the research. Y.Z., J.C., V.M., C.L.D., Y.Y. and S.L. performed the experiments. D.N., G.D.F., B.R. and W.L. analysed the results. X.L. performed the analysis of PLIN3 association with LDs. D.N. and G.D.F. wrote the paper. B.R., W.L., Q.S., Q.H. and P.X. edited and commented on the manuscript.

Competing interests

The authors declare no competing interests.

Additional information

Extended data is available for this paper at https://doi.org/10.1038/s42255-024-01085-w.

Supplementary information The online version contains supplementary material available at https://doi.org/10.1038/s42255-024-01085-w.

Correspondence and requests for materials should be addressed to Wei Liu, Brian Raught, Gregory D. Fairn or Dante Neculai.

Peer review information *Nature Metabolism* thanks Xun Huang, Maurine Linder and Douglas Mashek for their contribution to the peer review of this work. Primary Handling Editor: Yanina-Yasmin Pesch, in collaboration with the *Nature Metabolism* team.

Reprints and permissions information is available at www.nature.com/reprints.

Publisher's note Springer Nature remains neutral with regard to jurisdictional claims in published maps and institutional affiliations.
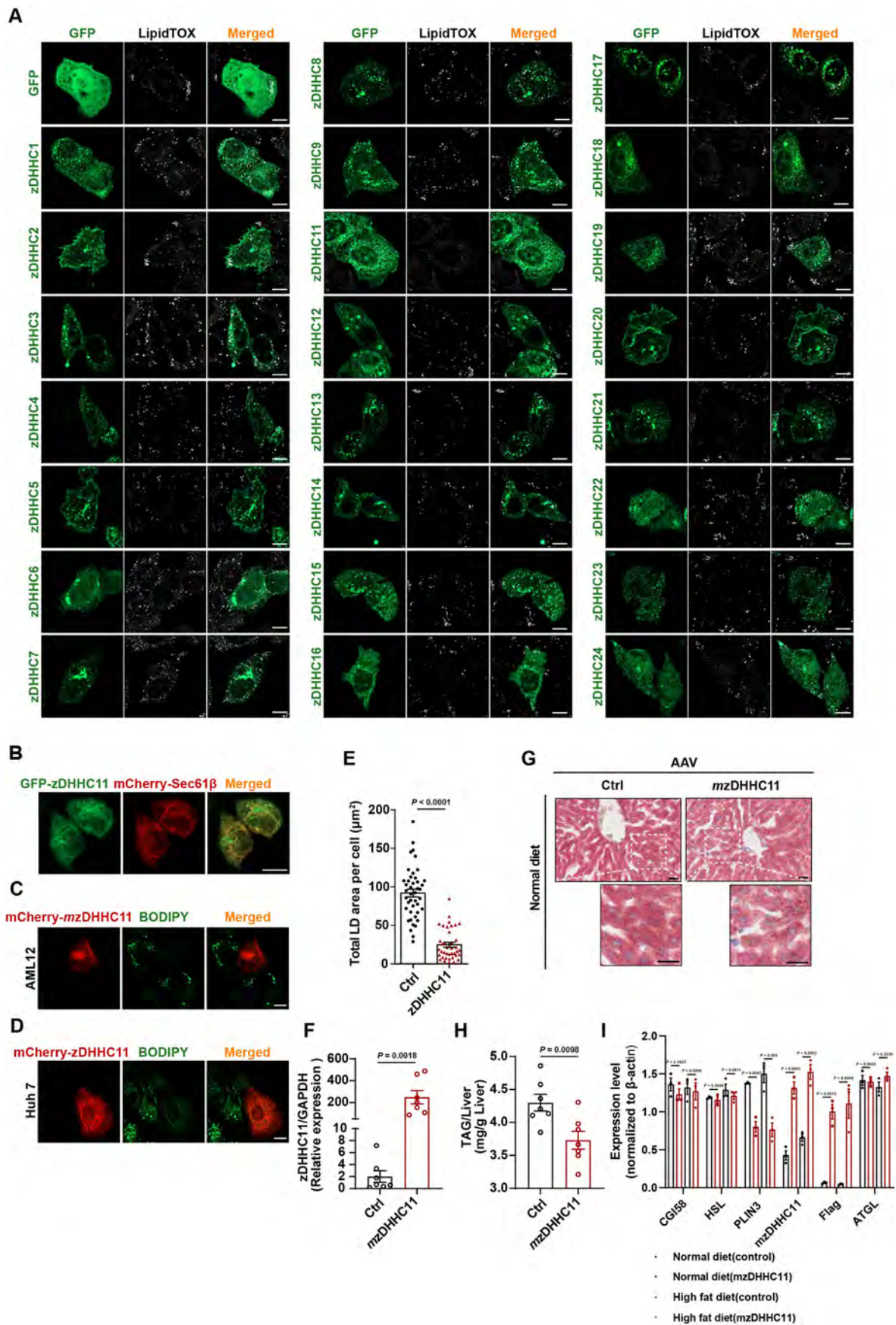
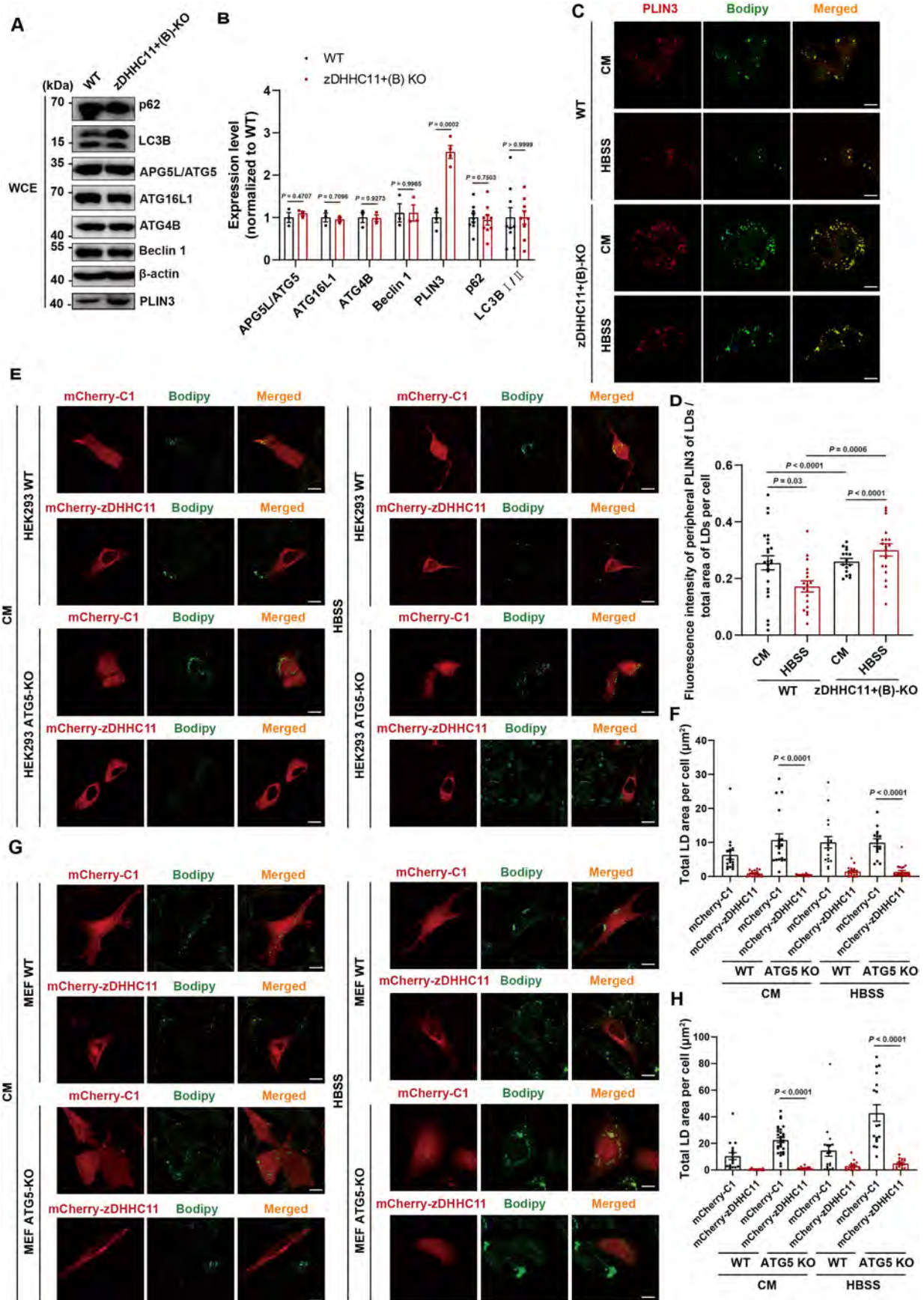**Extended Data Fig. 1 | See next page for caption.**

Extended Data Fig. 1 | Overexpression of zDHHC11 eliminates LDs in liver cells. (**a**) Fluorescence microscopy images depicting HepG2 cells either expressing GFP alone or GFP-tagged zDHHC family proteins. Lipid droplets (LDs) are highlighted using LipidTOX Red staining. (**b**) Confocal images displaying the subcellular localization of GFP-tagged zDHHC11 in HepG2 cells. These cells were co-transfected with an ER marker, mCherry-Sec61β. (**c**–**d**) Fluorescence microscopy images of AML12 (C) and Huh7 (D) cells expressing mCherry-tagged zDHHC11. In these images, LDs are stained using BODIPY 493/503. (**e**) Graph depicting the quantification of the total LD area per cell derived from data in (D). This includes data from three independent experiments, with n = 43 for control cells and n = 39 for Huh7 cells transiently expressing zDHHC11. (**f**) RT-qPCR analysis to determine zDHHC11 expression levels in female mouse livers. These mice were injected with either AAV-control virus or AAV-*m*zDHHC11

virus and maintained on a normal diet, with sample sizes of (n = 7 per group). (**g**) Representative liver sections from C57BL/6 J mice described in (F) stained with Oil Red O. (**h**) Quantification of total triglyceride content in liver samples from the mice described in (F) (n = 7 per group). (**i**) Densitometric analysis of the immunoblots shown in Fig. 1m, depicting the relative protein levels of CGI-58, HSL, PLIN3, zDHHC11, and ATGL in individual mouse liver samples. The protein levels were quantified by densitometry, normalized to the loading control β-actin, and each lane represents a separate biological replicate (individual mouse). Data in E, F, H, and I are presented as the mean ± SEM. Student's t-test was used to determine the significance of data in panels E, F, and H, while a one-way ANOVA and Tukey's post hoc test were applied to data in panel I. Scale bars for A-D are 10 μm and for G is 100 μm (with 100 μm insets).
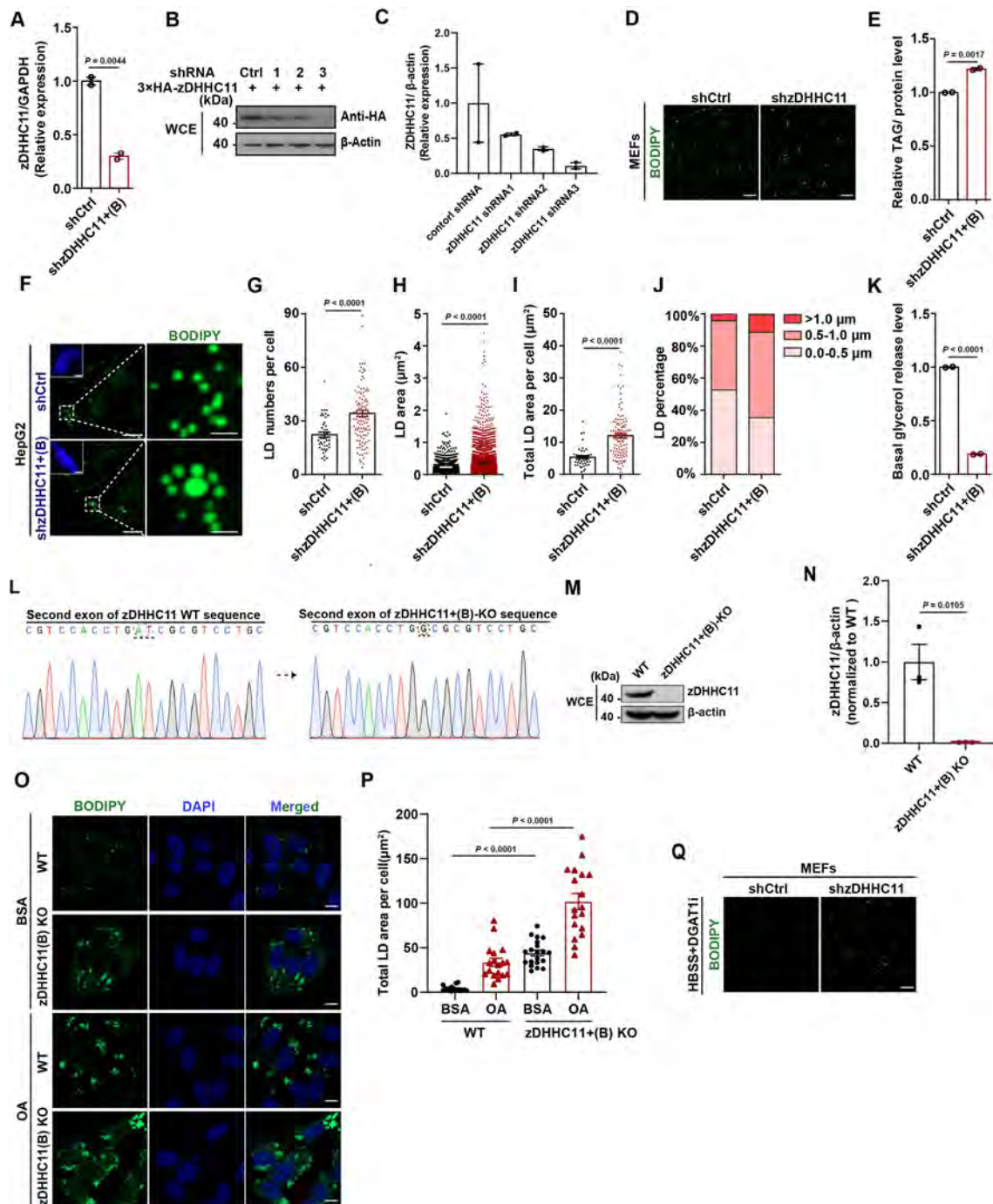
Extended Data Fig. 2 | Role of zDHHC11 in LD Metabolism. (a) RT-qPCR analysis showing zDHHC11 expression in MEFs. Reference is based on data from (C), (n = 2 independent repeats). **(b)** WB assessment of 3×HA-zDHHC11 in HEK293T cells transfected with control or three different zDHHC11-specific shRNA (n = 2 independent repeats). **(c)** Densitometric quantification of knockdown of the blots presented in (B). **(d)** Confocal images of MEF cells transduced with lentivirus expressing shRNA targeting zDHHC11 or control. LDs are stained using BODIPY 493/503. **(e)** Total triglycerides in MEFs are quantified in (C) (n = 2 independent repeats). **(f)** Confocal images of HepG2 cells transfected with either control or zDHHC11-specific shRNA. LDs are highlighted using BODIPY 493/503. **(g–i)** Quantification pertaining to HepG2 cells in (**f**): number of LDs (**g**), cross-sectional area of individual LDs (**h**), and total LD area (**i**). **(j)** Analysis of the percentage distribution of LD diameters from data in (E). Data was sourced from three independent experiments with sample sizes of n = 44 for shCtrl cells and n = 116 for shzDHHC11 + (B) cells. **(k)** Glycerol release measured in cells from

(F) (n = 2 independent repeats). **(l)** Sequencing of zDHHC11 + (B)-KO clones compared to the wild-type. **(m)** Representative immunoblot analysis showcasing zDHHC11 and β-actin levels in HepG2 and HepG2^zDHHC11+(B)-KO cells (n = 3 independent repeats). **(n)** Densitometric quantification of the blots presented in (M) illustrating knockout of zDHHC11. **(o)** Confocal images of HepG2 and HepG2^zDHHC11+(B)-KO cells after a 1-hour treatment with BSA or OA (100 μM). LDs stained with BODIPY. **(p)** Quantitative assessment of total LD area per cell from data in (O). Data sourced from three independent experiments with the following sample distributions: n = 16(HepG2+BSA), n = 20(HepG2^zDHHC11 + (B)-KO + BSA), n = 18(HepG2+OA), and n = 18(HepG2^zDHHC11 + (B)-KO + OA). **(q)** Confocal images of MEF-shCtrl and MEF-shzDHHC11 cells post a 24-hour incubation in HBSS with DGAT1i present. LDs stained with BODIPY, nuclei (DAPI). Data in (A, E, G, H, I, K, N, and P) are presented as mean ± SEM. Unpaired two-tailed Student's t-test applied to data in A, D, F, G, H and J. One-way ANOVA and Tukey's post hoc test were applied to data in N. All scale bars represent 10 μm.

**Extended Data Fig. 3 | See next page for caption.**

Extended Data Fig. 3 | ATG5-mediated lipophagy is dispensable for zDHHC11 enhanced lipolysis. (**a**) Representative immunoblot analysis of the indicated proteins in HepG2 and HepG2$^{zDHHC11+(B)-KO}$ cells (n = 3 independent repeats). (**b**) Densitometric quantification of immunoblots similar to (A). The analysis was based on independent experiments, with n = 9 for p62 and LC3B, and n = 4 for PLIN3. (**c**) Confocal images displaying endogenous PLIN3 proteins in HepG2 and HepG2$^{zDHHC11+(B)-KO}$ cells treated with CM medium and HBSS. LDs were visualized using BODIPY. (**d**) Quantification of peripheral PLIN3 fluorescence intensity on LDs, normalized by the total LD area of the same cell. Data sourced from cells in (C) incubated in CM (n = 24 for HepG2; n = 16 for HepG2$^{zDHHC11+(B)-KO}$) or after 24-hour incubation in HBSS (n = 18 for HepG2; n = 18 for HepG2$^{zDHHC11+(B)-KO}$) across three independent experiments. (**e**) Images of HEK293 and HEK293$^{ATG5-KO}$ cells expressing mCherry-C1 or mCherry-zDHHC11. Cells were incubated in either CM or HBSS for 24 hours. LDs are indicated with BODIPY 493/503 staining. (**f**) Quantification of (E). Data sourced from three independent experiments with the following sample sizes: HEK293-mCherry-C1 in CM: n = 18;

HEK293-mCherry-zDHHC11 in CM: n = 19; HEK293$^{ATG5-KO}$-mCherry-C1 in CM: n = 19; HEK293$^{ATG5-KO}$-mCherry-zDHHC11 in CM: n = 15; HEK293-mCherry-C1 in HBSS: n = 17; HEK293-mCherry-zDHHC11 in HBSS: n = 18; HEK293$^{ATG5-KO}$-mCherry-C1 in HBSS: n = 15; HEK293$^{ATG5-KO}$-mCherry-zDHHC11 in HBSS: n = 22). (**g**) Images of MEF and MEF$^{ATG5-KO}$ cells expressing mCherry-C1 or mCherry-zDHHC11 after 24-hour in CM or HBSS. LDs were visualized using BODIPY. (**h**) Quantification of total LDs area per cell in MEF and MEF$^{ATG5-KO}$ cells under different conditions and transfections as in (G). Data sourced from three independent experiments with the following sample sizes: MEF-mCherry-C1 in CM: n = 17; MEF-mCherry-zDHHC11 in CM: n = 16; MEF$^{ATG5-KO}$-mCherry-C1 in CM: n = 29; MEF$^{ATG5-KO}$-mCherry-zDHHC11 in CM: n = 20; MEF-mCherry-C1 in HBSS: n = 18; MEF-mCherry-zDHHC11 in HBSS: n = 18; MEF$^{ATG5-KO}$-mCherry-C1 in HBSS: n = 17; MEF$^{ATG5-KO}$-mCherry-zDHHC11 in HBSS: n = 180). Data in (B, D, F and H) represent mean ± SEM. Unpaired two-tailed Student's *t*-test applied to data in B. One-way ANOVA and Tukey's post hoc test was applied to data in D, F, and H. All scale bars represent 10 µm.
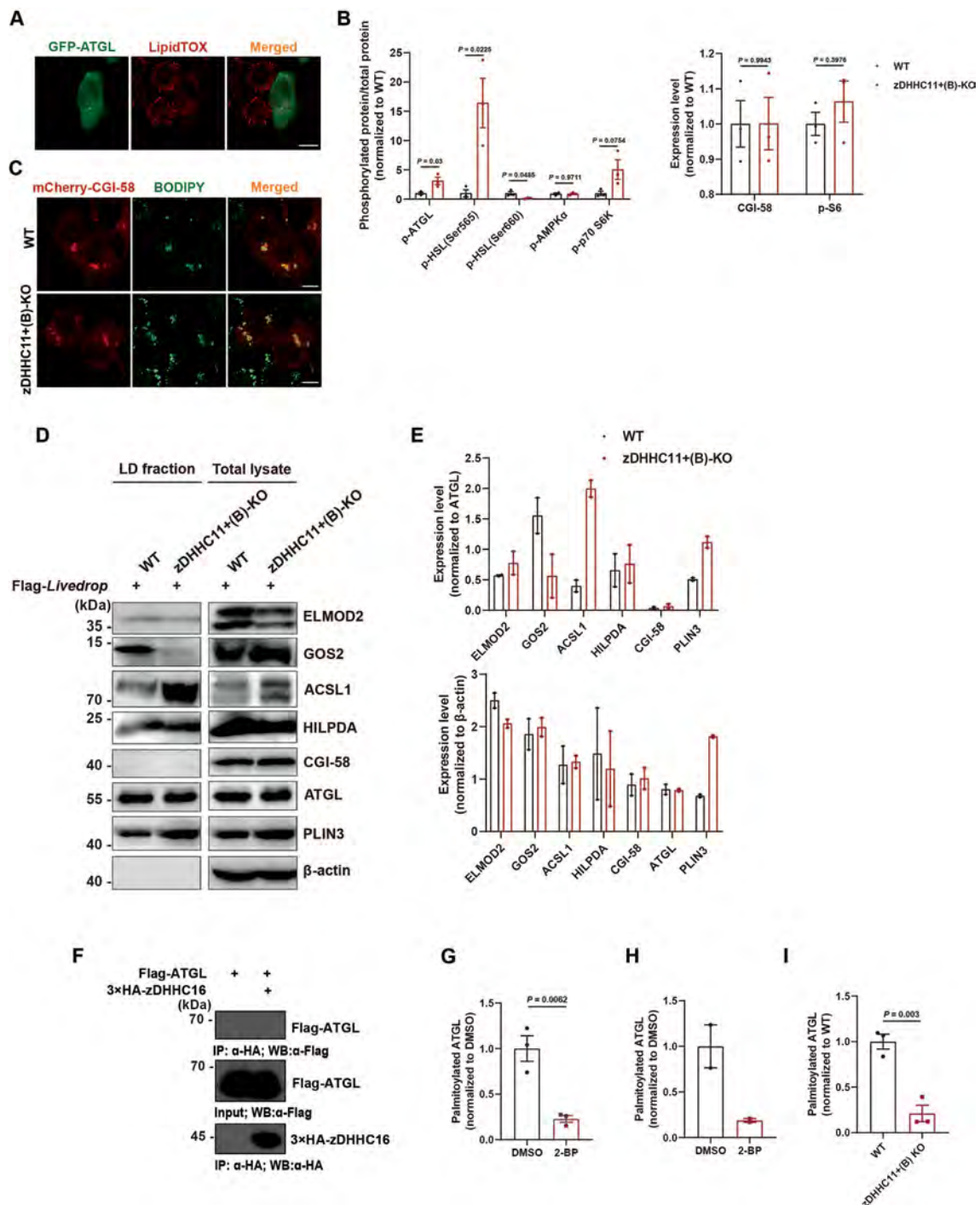
Extended Data Fig. 4 | Microscopy and immunoblot analysis of LD-associated proteins in wt and zDHHC11 + (B) ko HepG2 cells. (a) Confocal images of HepG2 cells expressing GFP-tagged ATGL. LDs were visualized using LipidTOX Red staining. **(b)** Densitometric quantification of the blots presented in Fig. 4a. **(c)** Fluorescence microscopy of HepG2 and HepG2^zDHHC11+(B)-KO cells expressing mCherry-tagged CGI-58. LDs were highlighted using BODIPY 493/503. **(d)** Representative immunoblot analysis of LD fractions and total lysates from HepG2 and HepG2^zDHHC1+(B)-KO cells expressing Flag-*Livedrop*. The blots were probed with antibodies against ELMOD2, G0S2, ACSL1, HILPDA, CGI-58, ATGL,

PLIN3, and β-actin (n = 2 independent repeats). **(e)** Densitometric quantification of the blots presented in (C), upper one corresponding to LD fraction(normalized to ATGL), nether one corresponding to total lysate(normalized to β-actin). **(f)** Co-immunoprecipitation of 3×HA-zDHHC16 and Flag-ATGL from HEK293T cells. Captured with anti-HA beads and immunoblotted. **(g, h, i)** Densitometric quantification of the blots presented in Fig. 4e–g, respectively. Data in (B, G, H, I) represent mean ± SEM. Unpaired two-tailed Student's t-test applied to data in (B, G, H, I). All scale bars represent 10 μm.
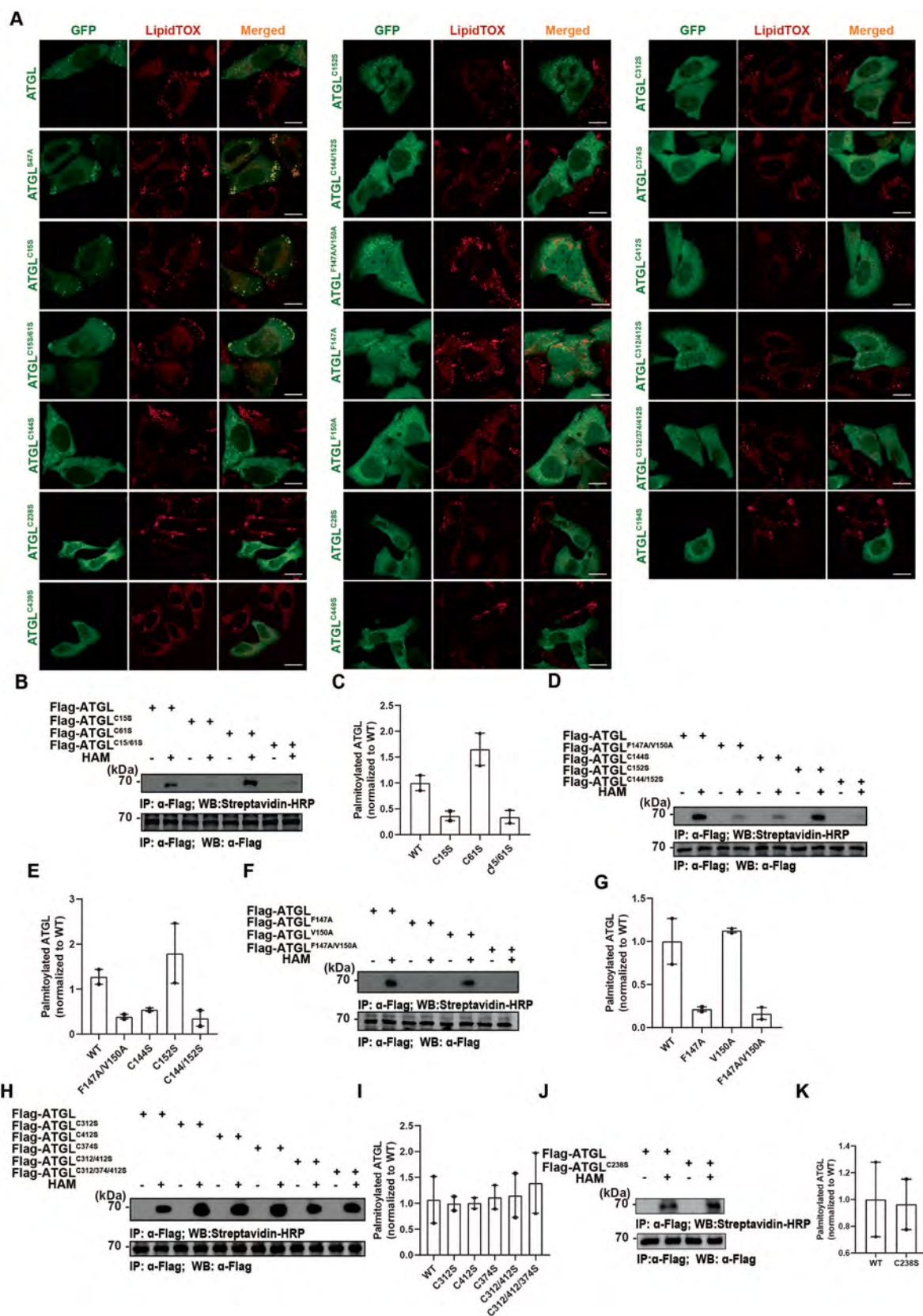
Extended Data Fig. 5 | Imaging and palmitoylation profiling of mutant ATGL proteins. (**a**) Confocal imaging of HepG2 cells expressing GFP-tagged ATGL mutants, as indicated. LDs were stained with LipidTOX Red. (**b, d, f, h, j**) Analysis of S-palmitoylation levels for Flag-tagged ATGL and mutants (as indicated) when expressed in HEK293T cells (n = 2 independent repeats). (**c, e, g, i, k**) Densitometric quantification of the blots presented in (**b, d, f, h, j**) respectively. All scale bars represent 10 μm.
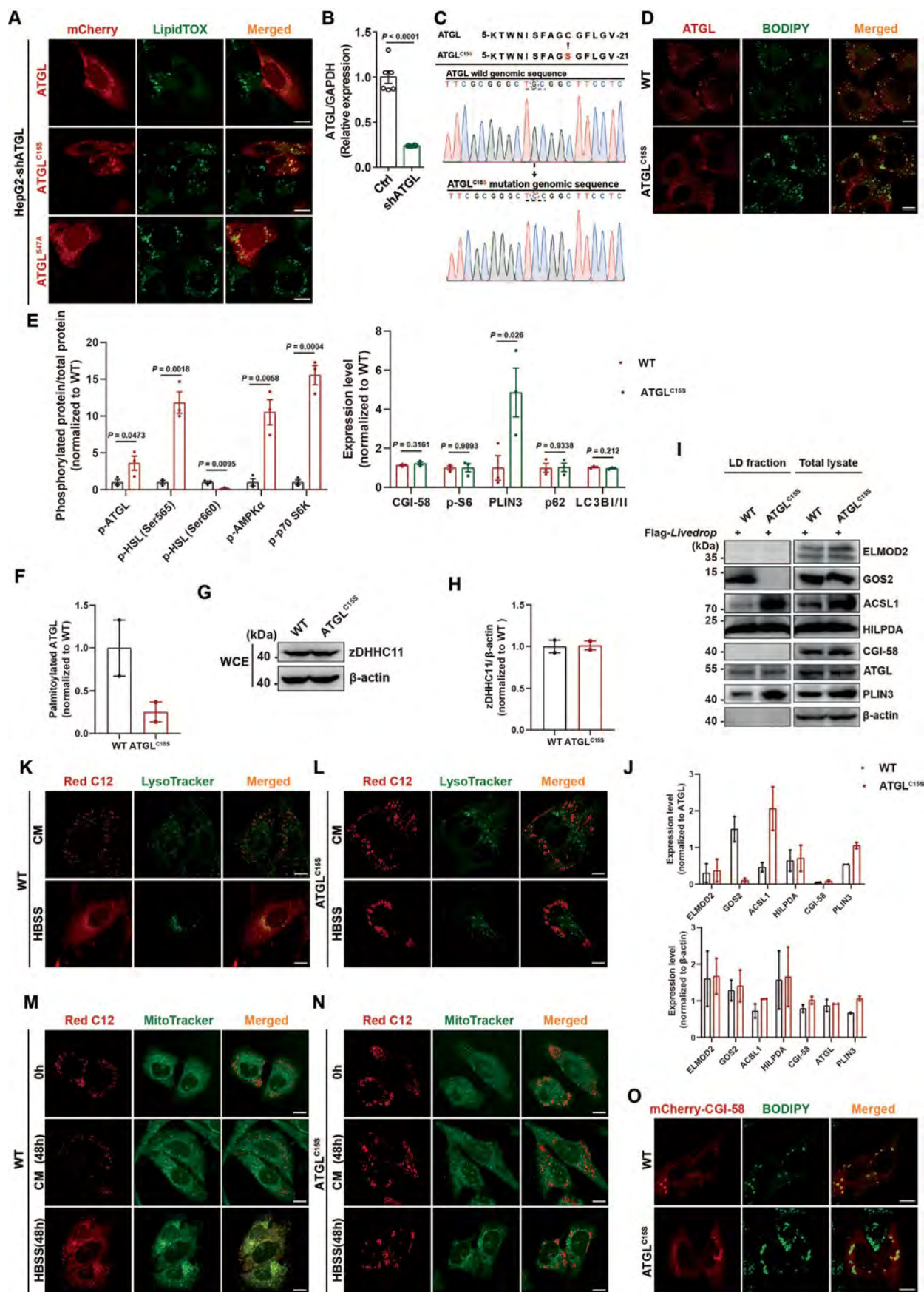
Extended Data Fig. 6 | See next page for caption.

Extended Data Fig. 6 | Palmitoylation-dependent regulation of ATGL targeting and LD-association. (**a**) Confocal images displaying mCherry-ATGL, mCherry-ATGL^{C15S}, and mCherry-ATGL^{S47A} in HepG2 cells following transduction with lentivirus expressing shRNA targeting ATGL's 3'UTR. LDs were visualized using LipidTOX Deep Red. (**b**) RT-qPCR assessment of ATGL expression in HepG2 cells after transduction with lentivirus either expressing shRNA targeting ATGL's 3'UTR or control lentivirus. (**c**) Sequencing of individual HepG2$^{ATGL.C15S}$ cell clones, aligned with the wild-type sequence. (**d**) Confocal imaging of endogenous ATGL in HepG2 and HepG2$^{ATGL.C15S}$ cells. LDs visualized using BODIPY 493/503. (**e** and **f**) Densitometric quantification of the blots presented in Fig. 5a, b, respectively. (**g**) Immunoblot analysis comparing zDHHC11 and β-actin expression between HepG2 and HepG2$^{ATGL.C15S}$ cells (n = 2 independent repeats). (**h**) Densitometric quantification of the blots presented in (E). (**i**) Representative immunoblot analysis of LD fractions and total lysates from HepG2 and HepG2$^{ATGL.C15S}$ cells expressing Flag-*Livedrop*. The blots were probed with antibodies against ELMOD2, G0S2, ACSL1, HILPDA, CGI-58, ATGL, PLIN3, and β-actin (n = 2 independent repeats). (**j**) Densitometric quantification of the blots presented in panel (G). The upper panel corresponds to the LD fraction, normalized to PLIN3, and the lower panel corresponds to the total lysate, normalized to β-actin (**k–l**) Confocal imaging of HepG2 and HepG2$^{ATGL.C15S}$ cells treated with Red C12, lysosomes labeled with LysoTracker. (**m–n**) Confocal images of HepG2 and HepG2$^{ATGL.C15S}$ cells treated with Red C12 as described in Fig. 3a, with mitochondria labeled using MitoTracker. (**o**) Fluorescence imaging displaying HepG2 and HepG2$^{ATGL.C15S}$ cells expressing mCherry-tagged CGI-58, with LDs stained with BODIPY 493/503. Data in E represent mean ± SEM. Unpaired two-tailed Student's *t*-test applied to data in E. All scale bars represent 10 μm.
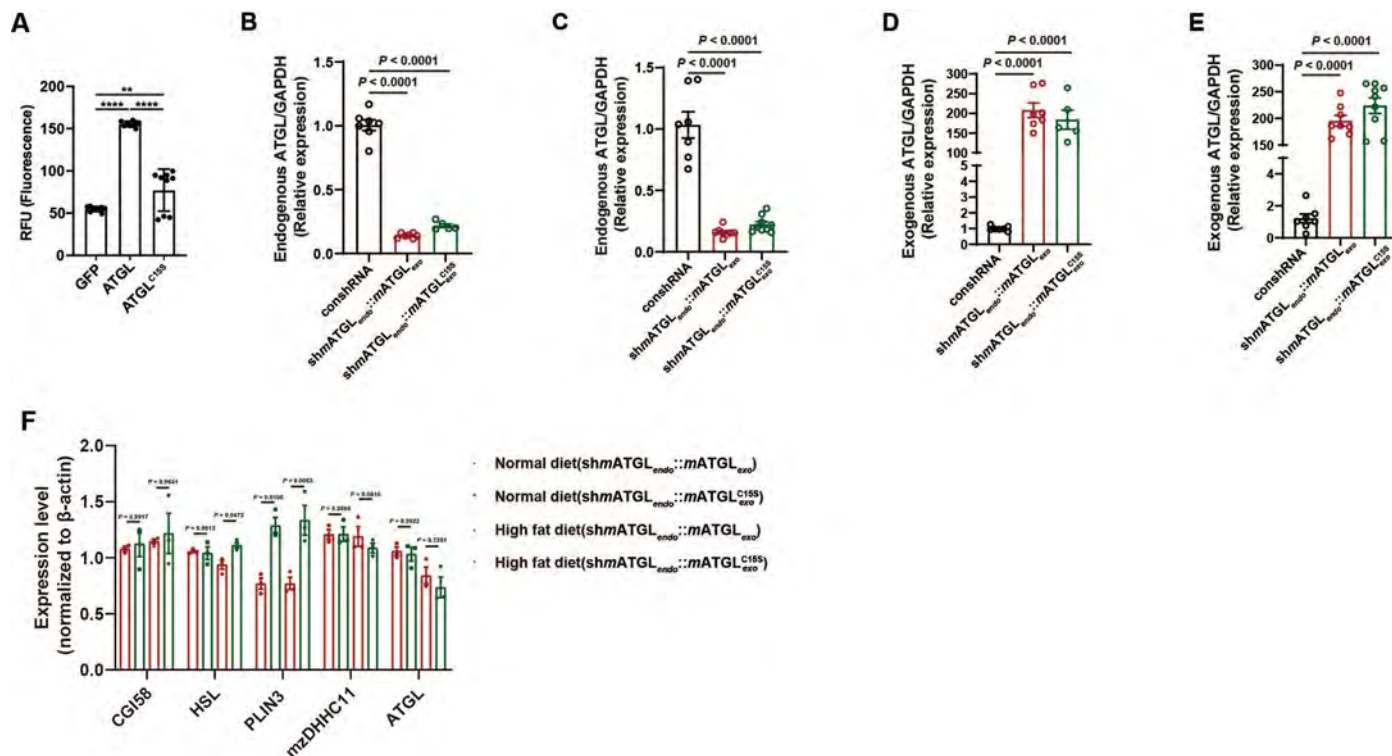
Extended Data Fig. 7 | Examining ATGL activity and hepatic expression in ATGL knockdown/rescue mouse model. (**a**) Fluorescence-based in vitro lipase activity assay of ATGL and ATGL^{C15S} proteins using EnzChek substrate. (**b**–**c**) RT-qPCR analysis assessing endogenous ATGL expression in C57BL/6 J mice from Fig. 5l–o, administered with AAV-shATGL$_{endo}$::mATGL$_{exo}$ or AAV-shATGL$_{endo}$::mATGL$^{C15S}_{exo}$ viruses and subsequently fed a normal diet (Fig. 5l,m) or a HFD (Fig. 5n,o). (**d**–**e**) RT-qPCR analysis showing exogenous ATGL expression in livers from mice in (Fig 5l,m) and (Fig 5n,o). (**f**) Densitometric quantification of the blots presented in Fig. 5p, illustrating the relative expression levels of CGI-58, HSL, PLIN3, zDHHC11, and ATGL. These levels are normalized to β-actin in liver samples from mice, with each lane representing one sample. Data in (**a**–**f**) represent mean ± SEM. Unpaired two-tailed Student's t-test applied to data in **f**. One-way ANOVA and Tukey's post hoc test was applied to data in **a**–**e**.

Corresponding author(s): Wei, Raught, Fairn, Neculai

Last updated by author(s): Jun 1, 2024

Reporting Summary

Nature Research wishes to improve the reproducibility of the work that we publish. This form provides structure for consistency and transparency in reporting. For further information on Nature Research policies, see Authors & Referees and the Editorial Policy Checklist.

Statistics

For all statistical analyses, confirm that the following items are present in the figure legend, table legend, main text, or Methods section.

n/a	Confirmed	
☐	☒	The exact sample size (*n*) for each experimental group/condition, given as a discrete number and unit of measurement
☐	☒	A statement on whether measurements were taken from distinct samples or whether the same sample was measured repeatedly
☐	☒	The statistical test(s) used AND whether they are one- or two-sided *Only common tests should be described solely by name; describe more complex techniques in the Methods section.*
☐	☒	A description of all covariates tested
☐	☒	A description of any assumptions or corrections, such as tests of normality and adjustment for multiple comparisons
☐	☒	A full description of the statistical parameters including central tendency (e.g. means) or other basic estimates (e.g. regression coefficient) AND variation (e.g. standard deviation) or associated estimates of uncertainty (e.g. confidence intervals)
☐	☒	For null hypothesis testing, the test statistic (e.g. *F*, *t*, *r*) with confidence intervals, effect sizes, degrees of freedom and *P* value noted *Give P values as exact values whenever suitable.*
☒	☐	For Bayesian analysis, information on the choice of priors and Markov chain Monte Carlo settings
☒	☐	For hierarchical and complex designs, identification of the appropriate level for tests and full reporting of outcomes
☒	☐	Estimates of effect sizes (e.g. Cohen's *d*, Pearson's *r*), indicating how they were calculated

Our web collection on statistics for biologists contains articles on many of the points above.

Software and code

Policy information about availability of computer code

Data collection	>>No new software nor code were used for data collection ZEN Blue(v 2.3), Lightcycler(v 2.0), OlyVIA(v 3.1.19668.0), Wave (v 2.6), Adobe Illustrator 2023 (v 27.0) , ImageCall (v 1.0.0000), Summit (v 6.3). QuantaSmart for liquid scintillation counting. Gen5 Software for measure fluorescence in microplate assays.
Data analysis	Fiji Software was used to analyze western blots and images. ZEN v3.6 (Zeiss) was used to analyze fluorescent micrographs. PixInsight software (https://pixinsight.com) was employed for signal analysis around the periphery of the LDs.

For manuscripts utilizing custom algorithms or software that are central to the research but not yet described in published literature, software must be made available to editors/reviewers. We strongly encourage code deposition in a community repository (e.g. GitHub). See the Nature Research guidelines for submitting code & software for further information.

Data

Policy information about availability of data

All manuscripts must include a data availability statement. This statement should provide the following information, where applicable:
- Accession codes, unique identifiers, or web links for publicly available datasets
- A list of figures that have associated raw data
- A description of any restrictions on data availability

The data that support the findings of this study are available from the corresponding authors upon reasonable request. A reporting summary for this Article is available as a Supplementary Information file. All source data, including additional replicate blots not illustrated in the main figures are provided as a Source Data file including uncropped and unprocessed scans of western blots.

Field-specific reporting

Please select the one below that is the best fit for your research. If you are not sure, read the appropriate sections before making your selection.

☒ Life sciences   ☐ Behavioural & social sciences   ☐ Ecological, evolutionary & environmental sciences

For a reference copy of the document with all sections, see nature.com/documents/nr-reporting-summary-flat.pdf

Life sciences study design

All studies must disclose on these points even when the disclosure is negative.

Sample size	Sample sizes were based on comparable previous studies but not strictly predetermined using statistical methods. This was further guided by the variability of measurements within and across repeated trials.
Data exclusions	Only exclusions have been made in case of failed experimental procedures (based on pre-established criteria)
Replication	All experiments supporting the main conclusions of this study have been successfully replicated multiple times using both biological and technical replicates, as indicated in the figure legends and corroborated by several models
Randomization	Samples and organisms were randomly allocated to experimental groups. No specific randomization protocol has been used. Mice were age- and sex matched.
Blinding	Investigators were not blinded to treatment allocation during experiments or outcome assessments due to the large number of experimental modalities and conditions that required specific knowledge of inherent variables (e.g. fluorophores, transfection, knockouts, treatments) and due to resource limitations.

Reporting for specific materials, systems and methods

We require information from authors about some types of materials, experimental systems and methods used in many studies. Here, indicate whether each material, system or method listed is relevant to your study. If you are not sure if a list item applies to your research, read the appropriate section before selecting a response.

Materials & experimental systems

n/a	Involved in the study
☐	☒ Antibodies
☐	☒ Eukaryotic cell lines
☒	☐ Palaeontology
☐	☒ Animals and other organisms
☒	☐ Human research participants
☒	☐ Clinical data

Methods

n/a	Involved in the study
☒	☐ ChIP-seq
☐	☒ Flow cytometry
☒	☐ MRI-based neuroimaging

Antibodies

Antibodies used	Primary antibodies, including supplier, dilutions, catalogue number, RRID and times used in open literature.
	Antibodies purchased from Cell Signaling Technologies
	Phospho-S6 Ribosomal Protein (Ser240/244)(5364)(for WB, 1:1000) RRID:AB_10694233 used >150 times
	ATGL (2138)(for WB, 1:1000), RRID:AB_2167955 used 32 times
	Phospho-Akt (Ser473)(4060)(for WB, 1:1000), RRID:AB_2315049 used >500 times
	Akt (pan) (C67E7)(4691)(for WB, 1:1000), RRID:AB_915783 used >400 times
	HSL (4107)(for WB, 1:1000), RRID:AB_2296900 used >66 times
	Phospho-AMPKα (Thr172)(2535)(for WB, 1:1000), RRID:AB_331250 used >360 times
	Phospho-HSL (Ser565) (4137)(for WB, 1:1000), RRID:AB_2135498 used 9 times
	Phospho-HSL (Ser660)(45804)(for WB, 1:1000), RRID:AB_2893315 used 3 times
	AMPKα (2532)(for WB, 1:1000), RRID:AB_330331 used >200 times
	p70 S6 Kinase(9202)(for WB, 1:1000), RRID:AB_331676 used >150 times
	LAMP1 (D2D11)(9091)(for WB, 1:1000), RRID:AB_2687579used 92 times
	Phospho-p70 S6 Kinase (Thr389)(9205)(for WB, 1:1000), RRID:AB_330944 used >150 times
	ACSL1(4047)(for WB, 1:1000) RRID:AB_2222411 used 3 times.
	From Abcam:
	Abhd5/CGI-58 antibody (ab183739)(for WB, 1:1000), RRID:AB_2909444 used 1 time
	Adipose Triglyceride Lipase (phospho S406) (ab135093)(for WB, 1:1000), RRID:AB_2888660 used 1 time

LSDP5 antibody (ab222811)(for WB, 1:1000), no RRID available used 3 times
CPT1A antibody (ab128568)(for WB, 1:1000), RRID:AB_11141632 used 26 times
APG5L/ATG5 antibody (ab108327)(for WB, 1:1000), RRID:AB_2650499 used 19 times
ATG16L1 antibody (ab187671)(for WB, 1:1000), No RRID, used 14 times and KO validated
ATG4B antibody (ab154843)(for WB, 1:1000), No RRID, used 6 times and KO validated
LC3B antibody (ab192890)(for WB, 1:1000) RRID:AB_2827794 used 28 times

From Novus:

Anti-ATGL(NBP2-59390)(for WB, 1:1000), no RRID, vendor validated
Anti-ABDH5 (H00051099-M01)(for WB, 1:1000) RRID:AB_536536 used 1 time

From Progen:

PLIN3 antibody (GP30)(for IF, 1:100) RRID:AB_2920671, vendor validated

From ProteinTech
P62/SQSTM1 Polyclonal antibody (18420-1-AP)(for WB, 1:1000) RRID:AB_10694431 used 40 times

From HuanAn Biotechnology (Huabio)

β-Actin (M1210-2)(for WB, 1:1000), RRID:AB_3073045 no citations.
GAPDH (EM1101)(for WB, 1:1000), RRID:AB_2811078 used 4 times

From BBI Life Sciences
PLIN3 antibody (D194875)(for WB, 1:1000); no RRID, vendor validated.

From LS Bio
HILPDA antibody (LS-C144423)(for WB, 1:1000) no RRID, vendor validated.

From Aviva Systems Biology
zDHHC11 Antibody (OAGA02799)(for WB, 1:1000) no RRID, vendor validated.

From Abclonal
ELMOD2 antibody (A7859)(for WB, 1:1000) RRID:AB_2769306, no citations

From Sigma
Monoclonal ANTI-FLAG M2 antibody (F1804)(for WB, 1:2000) RRID:AB_262044 used >500 times

From Thermo Fisher Scientific
zDHHC11 Antibody (PA5-69643)(for WB, 1:500), RRID:AB_2690108 no citations
G0S2 antibody (PA5-109748)(for WB, 1:1000). RRID:AB_2855159 no citations
Secondary antibodies:

Streptavidin-HRP conjugated (A0303)(for WB, 1:5000) was purchased from Beyotime;

Anti-HA-tag mAb-HRP-DirecT (M180-7)(for WB, 1:5000), Anti-DDDDK-tag mAb-HRP-DirecT (M185-7)(for WB, 1:5000), Anti-IgG (H+L chain) (Rabbit) (458)(for WB, 1:5000) and Anti-IgG (H+L chain) (Mouse) (330)(for WB, 1:5000) were purchased from MBL;

Anti-Rabbit IgG (Fc), AP Conjugate (S3731)(for WB, 1:5000), and Anti-Mouse IgG (H+L), AP Conjugate (S3721)(for WB, 1:5000) were purchased from Promega;

Goat anti-Mouse IgG (H+L) Highly Cross-Adsorbed Secondary Antibody (Alexa Fluor Plus 488) (A32723)(for IF, 1:200), Goat anti-Rabbit IgG (H+L) Highly Cross-Adsorbed Secondary Antibody (Alexa Fluor Plus 488) (A32731)(for IF, 1:200), Goat anti-Mouse IgG (H+L) Cross-Adsorbed ReadyProbes Secondary Antibody (Alexa Fluor 594) (R37121)(for IF, 1:200), Goat anti-Rabbit IgG (H+L) Cross-Adsorbed ReadyProbes Secondary Antibody (Alexa Fluor 594) (R37117)(for IF, 1:200) and Goat anti-Guinea Pig IgG (H+L) Highly Cross-Adsorbed Secondary Antibody (Alexa Fluor 594)(A-11076)(for IF, 1:200) were purchased from Thermo Fisher.

Validation

All commercial antibodies were validated by manufacturer and in some cases in other papers.

The validation information on their webpages are listed below:
Phospho-S6 Ribosomal Protein (Ser240/244) (D68F8) XP Rabbit mAb (CST, 5364); Suitable for: WB/IHC/IF/F; Reacts with: Human, Mouse, Rat, Monkey
https://www.cellsignal.com/products/primary-antibodies/phospho-s6-ribosomal-protein-ser240-244-d68f8-xp-rabbit-mab/5364

ATGL Antibody (CST, 2138); Suitable for: WB/IP/IF; Reacts with: Human, Mouse
https://www.cellsignal.com/products/primary-antibodies/atgl-antibody/2138

Phospho-Akt (Ser473) (D9E) XP Rabbit mAb (CST, 4060); Suitable for: WB/IP/IHC/IF/F; Reacts with: Human, Mouse, Rat, Hamster, Monkey, D. melanogaster, Zebrafish, Bovine
https://www.cellsignal.com/products/primary-antibodies/phospho-akt-ser473-d9e-xp-rabbit-mab/4060

Akt (pan) (C67E7) Rabbit mAb (CST, 4691); Suitable for: WB/IP/IHC/IF/F; Reacts with: Human, Mouse, Rat, Monkey, D.

melanogaster
https://www.cellsignal.com/products/primary-antibodies/akt-pan-c67e7-rabbit-mab/4691

HSL Antibody (CST, 4107); Suitable for: WB/IP/IF; Reacts with: Human, Mouse
https://www.cellsignal.com/products/primary-antibodies/hsl-antibody/4107

Phospho-AMPKα (Thr172) (40H9) Rabbit mAb (CST, 2535); Suitable for: WB/IP/IHC; Reacts with: Human, Mouse, Rat, Hamster, Monkey, D. melanogaster, S. cerevisiae
https://www.cellsignal.com/products/primary-antibodies/phospho-ampka-thr172-40h9-rabbit-mab/2535

Phospho-HSL (Ser565) Antibody (CST, 4137); Suitable for: WB/IF; Reacts with: Mouse
https://www.cellsignal.com/products/primary-antibodies/phospho-hsl-ser565-antibody/4137

Phospho-HSL (Ser660) Antibody (CST, 45804); Suitable for: WB; Reacts with: Human, Mouse
https://www.cellsignal.com/products/primary-antibodies/phospho-hsl-ser660-antibody/45804

AMPKα Antibody (CST, 2532); Suitable for: WB/IP; Reacts with: Human, Mouse, Rat, Hamster, Monkey
https://www.cellsignal.com/products/primary-antibodies/ampka-antibody/2532

p70 S6 Kinase Antibody (CST, 9202); Suitable for: WB/IP; Reacts with: Human, Mouse, Rat, Monkey
https://www.cellsignal.com/products/primary-antibodies/p70-s6-kinase-antibody/9202

LAMP1 (D2D11) XP Rabbit mAb (CST, 9091); Suitable for: WB/IP/IHC/IF/F; Reacts with: Human, Monkey
https://www.cellsignal.com/products/primary-antibodies/lamp1-d2d11-xp-rabbit-mab/9091

Phospho-p70 S6 Kinase (Thr389) Antibody (CST, 9205); Suitable for: WB; Reacts with: Human, Mouse, Rat, Monkey
https://www.cellsignal.com/products/primary-antibodies/phospho-p70-s6-kinase-thr389-antibody/9205

ACSL1 antibody (CST, 4047); Suitable for: WB/IHC; Reacts with: Human, Mouse, Rat
https://www.cellsignal.com/products/primary-antibodies/acsl1-antibody/4047

Abhd5/CGI-58 antibody (abcam, ab183739); Suitable for: Flow Cyt/WB/IHC-P; Reacts with: Human Predicted: Mouse
https://www.abcam.cn/products/primary-antibodies/abhd5cgi-58-antibody-epr12621-ab183739.html

Adipose Triglyceride Lipase (phosphor S406) (abcam, ab135093); Suitable for: WB/Elisa; Reacts with: Mouse Predicted:Rat, Dog, Pig, Chinese hamster
https://www.abcam.cn/products/primary-antibodies/adipose-triglyceride-lipase-phospho-s406-antibody-ab135093.html

LSDP5 antibody (abcam, ab222811); Suitable for: WB/ICC/IF; Reacts with: Human, Mouse
https://www.abcam.cn/products/primary-antibodies/lsdp5-antibody-ab222811.html

CPT1A antibody (abcam, ab128568); Suitable for: Flow Cyt/IHC-P/WB/ICC/IF/In-Cell ELISA; Reacts with: Human, Mouse, Rat
https://www.abcam.cn/products/primary-antibodies/cpt1a-antibody-8f6ae9-ab128568.html

APG5L/ATG5 antibody (abcam, ab108327); Suitable for: ICC/IF/WB/IP/IHC-P; Reacts with: Human, Mouse, Rat
https://www.abcam.cn/products/primary-antibodies/apg5latg5-antibody-epr17552-ab108327.html

ATG16L1 antibody (abcam, ab187671); Suitable for: WB/IHC-P; Reacts with: Human, Mouse, Rat
https://www.abcam.cn/products/primary-antibodies/atg16l1-antibody-epr15638-n-terminal-ab187671.html

ATG4B antibody (abcam, ab154843); Suitable for: Flow Cyt (Intra)/WB; Reacts with: Human, Mouse
https://www.abcam.cn/products/primary-antibodies/atg4b-antibody-epr64362-ab154843.html

LC3B antibody (abcam, ab192890); Suitable for: IHC-P/WB/ICC/IF; Reacts with: Human, Mouse, Rat
https://www.abcam.cn/products/primary-antibodies/lc3b-antibody-epr18709-autophagosome-marker-ab192890.html

PEDFR/PNPLA2/ATGL Antibody (Novus, NBP2-59390); Suitable for: WB/ELISA/Flow/ICC/IF; Reacts with: Human
https://www.novusbio.com/products/pedfr-pnpla2-atgl-antibody-at18e6_nbp2-59390

ABDH5 antibody (Novus, H00051099-M01); Suitable for: WB/ELISA/ICC/IF/IHC/KO; Reacts with: Human, Mouse, Rat, Bovine, Primate
https://www.novusbio.com/products/abhd5-antibody-1f3_h00051099-m01

PLIN3 antibody (progen, GP30); Suitable for: ICC/IF/IHC/WB; Reacts with: Human, Mouse, Rat
https://www.progen.com//anti-Perilipin-3-N-terminus-guinea-pig-polyclonal-serum/GP30

P62/SQSTM1 Polyclonal antibody (proteintech, 18420-1-AP); Suitable for: WB/IP/IF/FC/IHC/ELISA; Reacts with: Human, Goat, Chicken, Goslings, Monkey, Rabbit, Zebrafish, Hamster, Pig, Duck
https://www.ptglab.com/products/SQSTM1-Antibody-18420-1-AP.htm

β-Actin (HuaAn Biotechnology , M1210-2); Suitable for: WB/IHC(P)/ICC/IF/FLOW; Reacts with: Human, Mouse, Rat
http://www.huabio.cn/products/beta-Actin-antibody-M1210-2

GAPDH (HuaAn Biotechnology , EM1101); Suitable for: WB/IF/IHC-P; Reacts with: Human, Mouse, Rat, Zebrafish, Rabbit
http://www.huabio.cn/products/GAPDH-antibody-EM1101

PLIN3 antibody (BBI Life Science, D194875); Suitable for: WB/IF/FLOW; Reacts with: Human
https://store.sangon.com/productDetail?productInfo.code=D194875

HILPDA antibody (LS Bio, LS-C144423); Suitable for: WB/ELISA; Reacts with: Human, Mouse
https://www.lsbio.com/antibodies/hilpda-antibody-hig2-antibody-elisa-wb-western-ls-c144423/149281

zDHHC11 Antibody (Aviva systems biology, OAGA02799); Suitable for: IHC-P/WB; Reacts with: Human
https://www.avivasysbio.com/zdhhc11-antibody-oaga02799.html

ELMOD2 antibody (Abclonal, A7859); Suitable for: WB/ELISA; Reacts with: Human, Mouse
https://abclonal.com.cn/catalog/A7859

Monoclonal ANTI-FLAG M2 antibody (Millipore Sigma, F1804); Suitable for: WB/IHC/ICC/IF/FLOW/ELISA/IP/CHIP/ARRAY/GS;
Reacts with: all
https://www.sigmaaldrich.cn/CN/zh/search/f1804?
focus=products&page=1&perpage=30&sort=relevance&term=F1804&type=product

zDHHC11 Antibody (Thermo Fisher, PA5-69643); Suitable for: WB; Reacts with: Rat
https://www.thermofisher.cn/cn/zh/antibody/product/ZDHHC11-Antibody-Polyclonal/PA5-69643

G0S2 antibody (PA5-109748); Suitable for: WB/IHC; Reacts with: Human, Mouse, Rat
https://www.thermofisher.cn/cn/zh/antibody/product/G0S2-Antibody-Polyclonal/PA5-109748

Eukaryotic cell lines

Policy information about cell lines

Cell line source(s)	Huh7 and HEK293T cells were provided by the laboratory of Dr. Qiming Sun at the School of Basic Medical Sciences, Zhejiang University. HEK293, HepG2, HEK293 ATG5-KO, MEF, and MEF ATG5-KO cells were obtained from the laboratory of Dr. Wei Liu at the School of Basic Medical Sciences, Zhejiang University. 3T3-L1 were provided by the laboratory of Dr. Zhuoxian Meng at the School of Basic Medical Sciences, Zhejiang University. AML12 cells were obtained from the laboratory of Dr. Xiao Xu at the School of Basic Medical Sciences, Zhejiang University. ZDHCC11+(B)-KO HepG2 cells and ATGL.KI.C15S HepG2 cells were generated in the laboratory of Dr. Neculai.
Authentication	Cell lines were not independently authenticated
Mycoplasma contamination	The cells underwent regular testing, and all cell lines were confirmed to be free of mycoplasma contamination.
Commonly misidentified lines (See ICLAC register)	None of commonly misidentified cell lines has been used.

Animals and other organisms

Policy information about studies involving animals; ARRIVE guidelines recommended for reporting animal research

Laboratory animals	C57BL/6J mice of both sexes, aged 6-8 weeks at the start of experiments, were used. Mice were maintained on a 12-hour light/dark cycle with lights off at 7 AM. Animals had ad libitum access to standard chow diet or high-fat diet and water. Housing conditions were controlled at 22°C ± 2°C with 40% humidity.
Wild animals	No wild animals were used in the study
Field-collected samples	No field collected samples were used in the study.
Ethics oversight	All animal experiments were conducted in accordance with the guidelines and regulations approved by the Institutional Animal Care and Use Committee at Zhejiang University School of Medicine (AIRB-2021-1037).

Note that full information on the approval of the study protocol must also be provided in the manuscript.

Flow Cytometry

Plots

Confirm that:

☐ The axis labels state the marker and fluorochrome used (e.g. CD4-FITC).

☐ The axis scales are clearly visible. Include numbers along axes only for bottom left plot of group (a 'group' is an analysis of identical markers).

☐ All plots are contour plots with outliers or pseudocolor plots.

☐ A numerical value for number of cells or percentage (with statistics) is provided.

Methodology

Sample preparation	Employing the piggyBac system, we incorporated a GFP-Puromycin resistance fusion gene for positive and negative selection. HepG2 cells were co-transfected with the sgRNA-Cas9 plasmid and the donor plasmid. Seventy-two hours post-transfection, cells were trypsinized to create a single-cell suspension, and GFP-positive cells were sorted into 96-well plates.
Instrument	Beckman MoFloAstrios EQ flow cytometer
Software	Summit (v 6.3)
Cell population abundance	GFP cell sorting was performed.
Gating strategy	No extensive gating strategy was taken.

☐ Tick this box to confirm that a figure exemplifying the gating strategy is provided in the Supplementary Information.